PRDM16 restricts stem cell proliferation by integrating BMP and Wnt signalling in the developing choroid plexus

Li He[1], Jiayu Wen[2, *] and Qi Dai[1, *]

1 Department of Molecular Bioscience, the Wenner-Gren Institute, Stockholm University

2 Division of Genome Sciences and Cancer, The John Curtin School of Medical Research, The Australian National University

* Co-corresponding authors

Abstract

Cell proliferation, quiescence and differentiation are well balanced during organismal growth and tissue homeostasis. Understanding how such balance is achieved is crucial for tackling disease mechanisms such as those in cancer and neurological disorders. Here we have identified PRDM16 as a key regulator for BMP-induced neural stem cell (NSC) quiescence. PRDM16 acts as a co-repressor in the BMP pathway to repress cell proliferation genes. Such function of PRDM16 is required for the proper specification of choroid plexus (ChP) epithelial cells. Using a single-cell resolution fluorescent *in situ* approach, we show that NSC proliferation and Wnt pathway genes are abnormally elevated in the *Prdm16* mutant ChP. These findings uncover an essential function of PRDM16 in stem cell regulation, Wnt and BMP signalling. PRDM16 is a cell fate determinant in multiple tissue types. Our finding opens a possibility that PRDM16 uses similar strategies in relevant contexts and disease conditions.

Introduction

Uncontrollable cell proliferation can lead to tumor growth, while premature differentiation can result in tissue degeneration. How stem cell proliferation and quiescence are regulated is a fundamental question in developmental and stem cell biology. BMP (Bone morphogenetic proteins) signaling is a key cell-signaling pathway that plays a role in inducing and maintaining stem cell quiescence. Additionally, BMP signaling is involved in numerous cell specification processes (Zhang and Li, 2005).

The ability of a single pathway to play a diverse range of roles relies on context-specific transcriptional outputs. SMAD4 is the common transcription factor that mediates BMP and TGF-β/Activin signaling. Upon BMP induction, SMAD4 associates with phosphorylated SMAD1/5/8, while in response to TGF-β/or Activin, it complexes with phosphorylated SMAD2/3. It is known that the SMAD protein complexes can both activate and repress target gene expression. However, the precise mechanism that determines the regulatory activity of SMADs and target gene selection remains unclear (Hill, 2016).

In the mammalian brain, BMP and Wnt signaling pattern the brain midline where an essential structure, the ChP, emerges. Neural epithelial cells at the site of presumptive ChP lose neural potential, and the majority of them exit cell cycle. Only a few cells at the boarder of the ChP primordium and cortical hem (CH) remain as slowly dividing ChP progenitors which expand the monolayered ChP epithelial cells (Liddelow et al., 2010). BMP signaling is essential for ChP epithelium specification. Conditional depletion of the BMP receptor *BMPr1a* diminishes ChP development (Hebert et al., 2002), while ectopic BMP was sufficient to transform neural progenitors into ChP progenitors (Watanabe et al., 2012). Wnt signaling peaking at CH is also required for ChPe cell specification (al, 2020). Conditional depletion of ß-Catenin resulted in defective ChP, while overexpression of ß-Catenin expands CH at the expense of the ChP epithelium. These observations suggest that the level of Wnt and BMP signaling needs to be tightly controlled to ensure proper cell specification.

The PR domain-containing (PRDM) family protein PRDM16 determines cell fate specification in various cell types (Aguilo et al., 2011; Baizabal et al., 2018; Chui et al., 2020; Chuikov et al., 2010; Inoue et al., 2017; Kajimura et al., 2008; Shimada et al., 2017). Consistent with its essential roles in normal development, mutation and dysregulation of *Prdm16* are linked with several human diseases including those identified in the patients with 1p36 chromosomal

77 aberrations. It has been shown that deletion of *PRDM16* has a causal role in cardiomyopathy
78 (Arndt et al., 2013), while co-amplification of *PRDM16* and *SKI* was shown to promote tumour
79 growth via suppressing TGF-β anti-proliferation activity in gastric cancer cells (Takahata et al.,
80 2009). Moreover, as a master regulator of the thermogenic gene expression program in brown
81 adipocytes, PRDM16 has been studied as a promising target to treat obesity and other metabolic
82 diseases (Horvath and Scheele, 2022).

83 PRDM16 has versatile functions at the molecular level. It regulates chromatin accessibility and
84 epigenetic states of its bound enhancers (Baizabal et al., 2018; He et al., 2021), and depending
85 on the associated cofactors, PRDM16 can repress or activate gene expression. This poses a
86 challenge when targeting PRDM16 is a therapeutic strategy in disease treatment because
87 undesired outcome may occur. Thus, it is important to get a full understanding of the regulatory
88 roles of this protein in each individual process.

89 The ChP epithelium is directly specified from highly proliferative neural epithelium, making it
90 a tractable model to study mechanisms that regulate the transition between stem cell
91 proliferation and differentiation. Here we find that *Prdm16* mutant ChP cells fail to exit cell
92 cycle and were still proliferating NSCs. Further we show that PRDM16 collaborates with the
93 BMP pathway effectors, SMAD4 and pSMAD1/5/8, to suppress cell proliferating genes
94 including cell cycle regulators and Wnt signaling genes in quiescent NSCs. Finally, we
95 demonstrate that Wnt signaling and cell proliferation are abnormally elevated in the *Prdm16*
96 mutant ChP. Together, our work defines the mechanism by which PRDM16 functions in the
97 BMP pathway and suggests a regulatory circuit composed of BMP and Wnt signaling and
98 PRDM16 in the control of stem cell quiescence.

99

100

101

102

103

104

105 **Results**

106 ***Prdm16* is required for the specification of the ChP epithelium**

107 BMP signaling starts to specify the presumptive ChP at embryonic day E10.5 in mice (Hebert
108 et al., 2002) when *Prdm16* mRNAs become detectable in this region (**Fig. 1A**). Previously we
109 reported that animals of the *Prdm16* knockout (KO) null allele, *Prdm16*^{cGT} (*cGT*), show
110 severely reduced ChP structure (**Fig 1B)** (Bjork et al., 2010; He et al., 2021; Strassman et al.,
111 2017). In the *Prdm16* KO mutant, expression of the ChP marker gene, *Ttr*, is not only reduced
112 in the lateral ventricle (tChPs) but also in the fourth ventricle (hChP) (**Fig. 1C-D**), suggesting
113 that the function of PRDM16 is not area-restricted but generally required for ChP development.

114 To assess the overall patterning of the CH and ChP region, we checked expression of *Wnt2b*
115 and *BMP4* by conventional RNA *in situ* hybridization. The *Wnt2b* signal appeared normal in
116 mutant brains compared with the controls at E11.5 and E12.5 (**Supplementary Fig. 1A**),
117 suggesting that the area of CH was not affected by *Prdm16* deletion. Although the morphology
118 of *Prdm16* mutant ChP epithelium looked defective, as it remained as thick as the neural
119 epithelium, the level and range of *BMP4* expression in wild-type and mutant brains appeared
120 comparable (**Supplementary Fig. 1A**). This result indicates that loss of *Prdm16* does not affect
121 overall patterning of the medial-lateral region nor expression of *Wnt2b* and *BMP4*.

122 **Neural epithelial cells in the ChP primordium rely on PRDM16 to exit cell cycle and loss**
123 **neural potential**

124 Next, we attempted to examine cellular changes underlying defective ChP in the *Prdm16*
125 mutant. As the mutant ChP epithelium appeared thicker than the wild-type (**Fig. 1C-D**), we
126 examined cell proliferation of the ChP cells by a 2-hour EdU labeling at E12.5. In control
127 embryos from the same litter, the ChP cells were mostly EdU negative and transitioning into a
128 monolayer, suggesting that these cells have exited cell cycle. By contrast, *Prdm16* mutant ChP
129 cells remained highly proliferative (**Fig. 1E**).

130 To further check the property of *Prdm16* mutant ChP cells, we stained the control and mutant
131 brain slices with the neuronal marker Doublecortin (Dcx). The control brain lacked Dcx
132 positive cells in the ChP, suggesting that neural epithelial cells were specified into ChP
133 epithelial cells and thus lost neural potential (**Fig. 1F**). However, there were a number of Dcx

positive cells lining along the basal side of the epithelium in the *Prdm16* mutant ChP, indicative of continued neurogenesis.

To further examine the property of ChP cells, we stained the brain sections with the stem cell marker SOX2. SOX2 is highly expressed in NSCs adjacent to the ChP epithelium, but its expression became significantly reduced in the presumptive ChP area (**Supplementary Fig. 1C**). However, such reduction was abolished in the *Prdm16* mutant.

Together, these results demonstrate that *Prdm16* depletion disrupted the transition from neural progenitors into ChP epithelia, leading to ectopic proliferation and neurogenesis. This phenotype is a reminiscence of the BMP pathway mutant, Foxg1-cre::loxp*Bmpr1a,* where ectopic cell proliferation was found in the developing ChP (Hebert et al., 2002). We then wondered whether PRDM16 interacts with the BMP pathway to restrict cell proliferation.

PRDM16 and BMP signaling collaborate to induce NSC quiescence

It is known that BMP signaling maintains adult NSC quiescence and that BMPs are sufficient to induce cultured proliferative NSCs into quiescence (Mira et al., 2010). To determine how PRDM16 may interact with BMP signaling and regulates cell proliferation, we switched to using cultured primary NSCs (**Fig. 2A**). The PRDM16 protein is highly expressed in the nucleus of NSCs in embryonic brain tissues (**Fig. 1B**, and (He et al., 2021)). Unexpectedly, the protein becomes nearly undetectable when primary NSCs are cultured *in vitro* (**Supplementary Fig. 2A**) although *Prdm16* mRNA levels are still high (**Supplementary Fig. 2B**). This suggests that an unknown mechanism controls the stability and nuclear localization of PRDM16 *in vivo*. It was reported that post-translational modification of PRDM16 is an important regulatory switch for PRDM16 function in brown adipocytes (Wang et al., 2022). We speculate a similar mechanism is used in NSCs in the brain. To overcome this issue and examine potential molecular function of PRDM16 in NSC proliferation and gene regulation, we infected primary NSCs with a lenti-viral construct that constitutively expresses *3xNSL_Flag_Prdm16*, resulting in detectable PRDM16 protein in the nucleus and cytoplasm (**Supplementary Fig. 2A**). We referred this cell line as to *Prdm16_expressing (Prdm16_E)*. For comparison, we cultured NSCs from *Prdm16*_KO brains from the same developing stage and brain area.

Similar to previously reported (Mira et al., 2010), BMP4 was able to induce cell quiescence of proliferative *Prdm16_E*xpressing NSCs, as indicated by the reduction in the number of mKi67-

164 stained or EdU-labeled cells (**Fig. 2B-C**). By contrast, many of the *Prdm16*_KO cells failed to
165 exit cell cycle after BMP4 addition, evidenced by less reduction of the mKI67 or EdU positive
166 cell population (**Fig. 2B-C**) and reduced *mKi67* mRNA levels measured by reverse-
167 transcription followed by quantitative PCR (RT-qPCR) assay (**Fig. 2D**). Thus, similar to their
168 function in ChP specification, both BMP signaling and PRDM16 are required for inducing
169 NSCs to exit cell cycle. We then went forward to examine molecular function of PRDM16 and
170 BMP signaling in this context.

171 **PRDM16 assists genomic binding of the BMP pathway transcription factors**

172 As PRDM16 is a transcriptional regulator, we hypothesized that the interaction of PRDM16
173 and BMP signaling, if there is any, should occur at the genome. To this end, we monitored
174 changes of transcription factor binding in the genome during the transition of proliferation to
175 quiescence state. Using *Prdm16_E* and *Prdm16_KO* NSCs treated with BMP4 and those non-
176 treated, we performed CUT&TAG experiments with the PRDM16 antibody. As none of the
177 SMAD antibodies worked in CUT&TAG assays in our tests, we performed ChIP-seq with the
178 antibodies targeting all three classes of SMAD transcription factors including SMAD4,
179 SMAD3 and phosphorylated SMAD1/5/8. Thus, our experiment settings allow profiling of
180 PRDM16 binding sites together with SMAD binding sites induced by endogenous BMPs and
181 TGF-β/Activin and ectopic BMP4.

182 Using SEACR peak caller (Meers et al., 2019), we identified 3337 and 7639 PRDM16
183 CUT&TAG common peaks from four replicates of the BMP4-treated and non-treated
184 *Prdm16_E* samples (FDR < 10%, see Methods), respectively, representing PRDM16-bound
185 genomic sites at these two conditions (**Fig. 3A**). The samples from *Prdm16_KO* cells
186 completely lack these sites, validating the specificity of the PRDM16 CUT&TAG signal (**Fig.**
187 **3B**). There are 5936 lost and 1634 gained PRDM16 CUT&TAG peaks upon BMP4 treatment,
188 suggesting that PRDM16 regulates a distinct subset of genes in proliferating versus quiescent
189 NSCs.

190 In *Prdm16_E* cells without BMP4, we identified a few hundred to thousand ChIP-seq peaks for
191 all three classes of SMAD proteins after normalizing to the input reads (FDR < 10%),
192 suggesting a modest level of endogenous BMP and TGF-β signaling in these cells (**Fig. 3C,**
193 **Supplementary Fig. 3**). Following BMP4 addition, pSMAD1/5/8 gained around 750-fold
194 more peaks, while the number of SMAD3 peaks increased less than three folds (**Fig. 3D**,

195 **Supplementary Fig. 3A**). Moreover, in BMP4-treated cells pSMAD1/5/8 peaks largely
196 overlap with SMAD4 peaks, but not with the SMAD3 ones (**Supplementary Fig. 3B**). For
197 instance, pSMAD1/5/8 binding to two enhancers in the intronic region of *Prdm16* was
198 increased in response to BMP4 (**Supplementary Fig. 3D**). This means that *Prdm16* itself is a
199 transcriptional target of BMP signaling. We also noticed that *Prdm16* mRNA levels can be
200 elevated by BMP4 in wild-type but not *Prdm16_KO* cells (**Supplementary Fig. 2B**). SMAD3
201 showed little ChIP-seq signal here in the absence and presence of BMP4. These results are
202 consistent with the notion that pSMAD1/5/8 is the main receptor SMAD of BMP signaling
203 while SMAD3 is generally irresponsive to BMP4. The gained Smad3 sites may derive from
204 indirect effect of BMP signaling.

205 We then focused on assessing how PRDM16 influences genomic localization of the SMAD
206 proteins. In overlapping analyses (see Methods), we found that more than 50% of SMAD4 and
207 pSMAD1/5/8 binding peaks are consistent in *Prdm16_E* and *Prdm16_KO* cells
208 (**Supplementary Fig. 4A-B**), suggesting that deletion of *Prdm16* does not affect general
209 genomic binding ability of the SMAD4/pSMAD1/5/8 proteins. In *Prdm16_E* cells with BMP4,
210 most of PRDM16 CUT&TAG peaks overlap with the SMAD4 and pSMAD1/5/8 peaks, but
211 not much with SMAD3 (**Supplementary Fig. 4C**), suggesting that PRDM16 mainly
212 collaborates with the SMAD4/pSMAD1/5/8 complex at the condition with BMP4.

213 Interestingly, we found that the enrichment of SMAD4 and pSMAD1/5/8 at the PRDM16 co-
214 bound sites became significantly lower in *Prdm16*_KO mutant cells than that in *Prdm16_E*
215 cells (**Fig. 3D**) (P=2.5E-6, and P=4.7E-3, respectively, two-tailed *t*-test), suggesting that SMAD
216 binding to these sites depends on PRDM16. As a control, the sites without PRDM16 co-binding
217 did not show such change (P>0.05). Thus, PRDM16 localizes SMAD proteins at specific
218 genome regions.

219 We wondered whether there is any intrinsic difference between SMAD-bound regions with and
220 without PRDM16 binding. It has been shown that SMAD4 can bind to two major types of DNA
221 motifs (Hill, 2016): together with SMAD3, SMAD4 may bind to a palindromic motif,
222 GTCTAGAC or direct repeats of GTCT like GTCTGTCTGTCT (Dennler et al., 1998; Wong
223 et al., 1999; Zawel et al., 1998); together with pSMAD1/5/8, SMAD4 associates with GC-rich
224 SBEs (SMAD-binding elements) including GGCGCC-AN4-GNCV and
225 GRCGNCNNNNNGTCT (Gao et al., 2005; Pyrowolakis et al., 2004; Weiss et al., 2010). To
226 determine how PRDM16 may influence enhancer selection of SMADs, we calculated

occurrence frequency of each of these motifs in five bins of SMAD4 ChIP-seq peaks from Prdm16_E cells treated with BMP4 (bin 1 to 5 with low to high peak scores, **Fig. 3E**). Interestingly, the palindromic motif is the most enriched one, and its occurrence frequency increases with peak scores. Notably, the frequency is lower in SMAD4 peaks without PRDM16 co-binding. The other three motifs show a different trend: they are not as highly enriched, their frequencies do not increase with higher SMAD4 peak scores, and the occurrence frequency in PRDM16 co-bound regions is either comparable to or even lower than the regions without PRDM16 binding. This result suggests that PRDM16 mainly tethers the SMAD4/pSMAD1/5/8 complex to the regions enriched of the palindromic motif.

Two candidate target genes co-regulated by PRDM16 and SMADs are *Wnt7b* and *Id1* (**Fig. 3F, Supplementary Fig. 4D**). We confirmed that these proteins simultaneously bind to the same DNA molecules by using sequential ChIP-qPCR with the PRDM16 antibody in the first round of IP and the SMAD4 antibody in the second IP at the *Wnt7b* and *Id1* gene loci (**Supplementary Fig. 4E**). SMAD4 displayed higher enrichment in the chromatin pulled by the PRDM16 antibody compared to that by the IgG control. We also validated reduced SMAD binding at one SMAD/PRDM16 co-bound site from each of the *Wnt7b* and *Id1* loci by ChIP-qPCR with the SMAD4 antibody in *Prdm16_E* and *Prdm16_KO* cells. SMAD4 binding became consistently weaker in the mutant in two biological replicates (**Fig. 3G, Supplementary Fig. 4F**).

Our careful inspection on the *Wnt7b* and *Id1* loci revealed that there appeared multiple ectopic SMAD4 and pSMAD1/5/8 peaks in the *Prdm16* mutant (arrow-indicated peaks in **Fig. 3F** and **Supplementary Fig. 4D**). We then globally assessed the extent of ectopic SMAD binding surrounding the SMAD/PRDM16 co-bound sites by quantifying differential SMAD binding intensity between *Prdm16_KO* and *Prdm16_expressing* cells (**Fig. 3H, Supplementary Fig. 4G**) (FDR < 10%). In agreement with the metaplots (**Fig. 3D**), all of the SMAD/PRDM16 co-bound sites showed reduced coverage intensity in *Prdm16* mutant cells. By contrast, the flanking regions within the 200kb range of a co-bound site displayed a trend of increase of SMAD binding in *Prdm16* mutant cells. This result indicates that PRDM16 helps to localize the SMAD complex at specific *cis* regulatory elements and that without *Prdm16*, the SMAD factors are partly redirected to neighboring genomic regions.

AP1 is the potential co-factor that interacts with relocated SMAD proteins

257 We then wondered how SMAD4 and pSMAD1/5/8 relocate to ectopic sites in the absence of
258 *Prdm16*. By running *de novo* motif discovery (see Methods), we identified a handful
259 significantly enriched DNA motifs from pSMAD1/5/8 and SMAD4 ChIP-seq peaks in
260 *Prdm16_E* and *Prdm16_KO* cells (**Fig. 4A-B**). Interestingly, in addition to the known SMAD
261 motifs, the only other motif identified in both pSMAD1/5/8 and SMAD4 peaks from
262 *Prdm16_KO* cells but not *Prdm16_expressing* cells is the AP1 motif. Furthermore, the AP1
263 motif is found more frequently in the pSMAD1/5/8 and SMAD4 regions lacking PRDM16
264 binding than those with PRDM16 binding (**Fig. 4C**). The interaction between the AP-1 complex
265 with the SMAD proteins was reported previously (Zhang et al., 1998). Our result implies that
266 AP-1 is a potential cofactor for the SMAD proteins in the absence of *Prdm16*. To validate this
267 finding, we performed ChIP-qPCR with an antibody against c-FOS, one of the subunits of AP1,
268 on *Prdm16_E* and *KO* cells. Supporting the global analyses, c-FOS is enriched in the Smad4-
269 bound peaks at the *Wnt7b* and *Id3* loci in the *Prdm16_KO* condition (**Fig. 4 D-G**). There is no
270 or only weak c-FOS binding to these regions in cells expressing *Prdm16*, suggesting that there
271 is cooperativity of SMAD and AP-1 facilitating each other's binding when PRDM16 is absent.
272 Alternatively, PRDM16 may suppress genomic accessibility of these regions for SMAD and
273 AP-1 proteins, a function PRDM16 has in cortical NSCs (He et al., 2021).

274 **Genomic relocation of SMAD4/pSMAD de-represses cell proliferation genes**

275 Next, we assessed gene regulatory activities of PRDM16 and SMAD4/pSMAD co-binding. As
276 a start, we examined expression change of *Wnt7b* using RT-qPCR, and found a drastic reduction
277 of *Wnt7b* expression in *Prdm16*_E cells in response to BMP4. This suggests that a high level
278 of BMP signaling represses *Wnt7b*. PRDM16 also directly represses *Wnt7b*, as the *Prdm16*_KO
279 sample displayed higher *Wnt7b* expression than the *Prdm16_E* sample even without BMP4
280 addition. Importantly, expression of *Wnt7b* is no longer suppressed by BMP4 addition in
281 *Prdm16*_KO cells, suggesting that BMP signaling synergizes with PRDM16 to repress *Wnt7b*
282 (**Fig. 5A**).

283 To extend this finding to all PRDM16 and BMP co-regulated genes in NSCs, we determined
284 the state of transcription activation using the H3K4me3 CUT&TAG signal in BMP4-treated
285 and non-treated *Prdm16_E* and *Prdm16_KO* cells. It is known that cell identity genes are
286 marked by extended breadth of H3K4me3 (Benayoun et al., 2014). We reasoned that compared
287 to RNA-seq profiling that measure gene expression change for all genes, changes in the
288 H3K4me3 signal at the promoter may bias toward cell identity genes between proliferation and

289 quiescence states. First, we noticed that the change of H3K4me3 intensity at the *Wnt7b*
290 promoter faithfully recapitulated the change of *Wnt7b* mRNA levels shown by RT-qPCR (**Fig.**
291 **5B**). As a negative control, the TGF-β pathway target gene *Cdkn1a* encoding the cell cycle
292 inhibitor *p21* showed unchanged H3K4me3 coverage between BMP4 treated and non-treated
293 cells and between *Prdm16_E* and *KO* cells, suggesting that neither PRDM16 nor BMP
294 signaling affects expression of *Cdkn1a* in NSCs. Next, we determined all BMP4-repressed and
295 activated genes, by measuring changes of the H3K4me3 CUT&TAG read coverage at annotated
296 transcription starting sites (TSS) in BMP4-treated *Prdm16_E* cells versus those non-treated,
297 and identified 145 up-regulated and 184 down-regulated SMAD target genes (**Fig. 5C**)
298 ($P<0.01$). To identify PRDM16-repressed and activated genes in the condition of BMP4, we
299 called changes of H3K4me3 coverage at TSSs in *Prdm16_KO* cells treated with BMP4 versus
300 *Prdm16_E* cells treated with BMP4. There were about twice as many up-regulated genes as
301 down-regulated genes (**Fig. 5D**), suggesting that the cooperative activity of PRDM16 and BMP
302 signaling is mainly to repress target gene expression.

303 To identify the function of genes regulated by PRDM16 and BMP signaling, we performed
304 gene ontology (GO) analyses for genes that changed expression in response to BMP4 in
305 *Prdm16_E* cells (see Methods). Remarkably, only downregulated genes (BMP-repressed genes)
306 show significantly enriched functional categories, and nearly all GO terms are related to cell
307 proliferation/cell cycle (**Fig. 5E)**. A recent study reported that BMP2-induced genes are mostly
308 enriched for neuronal and astrocyte differentiation (Katada et al., 2021), while our analysis did
309 not identify these categories. The discrepancy may derive from difference in NSC culture, as
310 ours was from E13 instead of E11 and E14, or different profiling methods, H3K4me3 versus
311 RNA-seq. We overlapped these 184 genes with the 240 genes de-repressed in *Prdm16* mutant
312 cells and identified 31 common ones. These 31 genes all display low H3K4me3 coverage in
313 *Prdm16_E* cells with BMP4 but higher H3K4me3 signal in both *Prdm16_KO* cells treated with
314 BMP4 and *Prdm16_E* cells without BMP4 (**Fig. 5F).**

315 We then intended to determine direct targets among these 31 genes that are regulated via
316 PRDM16-bound enhancers. We previously showed that PRDM16 preferentially associates with
317 distal intergenic regions (He et al., 2021), posing a challenge of pairing the PRDM16-bound
318 enhancers to the targeting promoters. To overcome this issue, we took advantage of a public
319 data browser, Embryonic Mouse Brain Epigenome Atlas (Rhodes et al., 2022), where promoter-
320 enhancer pairs are predicted by the Monocle3 extension Cicero (Pliner et al., 2018). We

321 manually inspected all 31 genes for the presence of at least one PRDM16 CUT&TAG peak that
322 is associated with the gene promoter, and found that 23 of them have proximal or distal
323 PRDM16 binding peak(s) (**Fig. 5F,** text in back**).** Thus, these genes represent direct
324 transcriptional targets synergistically repressed by PRDM16 and BMP signaling.

325 Together, our genomic data and validation suggest an enhancer switch model (**Fig. 5G)**:
326 PRDM16 assists SMAD protein binding to repressive cis-regulatory elements that are enriched
327 for GTCTAGAC palindromic motifs; loss of PRDM16 results in genomic relocation of SMAD
328 proteins, presumably via the association with coactivators such as AP1; the consequence of
329 SMAD relocation is de-repression of cell proliferation regulators.

330 **SMADs and PRDM16 co-regulated genes in NSCs are expressed in the developing ChP**

331 Next, we intended to examine whether the genes co-regulated by PRDM16 and BMP signaling
332 in NSCs are involved in ChP development, an *in vivo* setting where BMP signaling (Hebert et
333 al., 2002) and PRDM16 (**Fig. 1**) restrict NSC proliferation. To address this, we first examined
334 expression of these genes in the developing mouse brain by taking advantage of the published
335 single cell RNA-seq (scRNA-seq) data (La Manno et al., 2021). We selected a number of E12.5
336 cell clusters based on marker gene expression, including the ChP epithelial cell clusters (*Ttr*
337 positive), CH clusters (BMP4 positive but *Ttr* negative) and a few forebrain-specific radial glia
338 (RG) clusters (Sox2/Hes5 positive) (**Fig. 6A**). Among the 31 genes, six show no expression,
339 and five have little expression in the examined clusters (**Supplementary Fig. 5A**). The
340 remaining twenty genes display a moderate to high level of expression in at least one cluster.
341 Interestingly, they are generally more lowly expressed in the ChP clusters than the CH and RG
342 ones (**Fig. 6A**), suggesting expression of these genes may be repressed in the ChP. To identify
343 which of these genes are directly regulated by PRDM16, we performed CUT&TAG assays
344 using the PRDM16 antibody on dissected dorsal midline tissue that mainly contains CH and
345 the ChP (**Fig 6B** and **Supplementary Fig. 5B**) and identified 3238 common peaks from three
346 biological replicates. We then manually inspected the 31 gene loci for PRDM16 CUT&TAG
347 peaks pairing with the target gene TSS using the browser Embryonic Mouse Brain Epigenome
348 Atlas (Rhodes et al., 2022). This conformed that most of these genes have at least one PRDM16
349 binding peak in their promoter-linked enhancers (Text in black, **Fig. 6A** and **Supplementary**
350 **Fig. 5A**).

351 Among these genes, *Wnt7b* is of particular interest, because the level of Wnt signaling was
352 shown to be critical for ChP specification (Parichha et al., 2022), and Wnt signaling promotes
353 proliferation of NSCs (Kalani et al., 2008). Although the sequencing coverage looks sparser
354 compared to that from NSC culture, there are two PRDM16 binding peaks identified within the
355 *Wnt7b* region (**Fig 6C**). The intronic peak is unique to the dorsal midline tissue, suggesting that
356 this enhancer may be specifically regulated in the developing ChP. Thus, *Wnt7b* is a potential
357 target of PRDM16 in the developing ChP.

358 **PRDM16 represses Wnt genes in the developing ChP**

359 We sought to determine whether PRDM16 regulates Wnt gene expression in the developing
360 ChP. In addition to *Wnt7b*, there are several other Wnt ligands expressed in the CH and ChP
361 region (Harrison-Uy and Pleasure, 2012). For example, *Wnt3a* is expressed in the dorsal-
362 midline region but not in the forebrain, which explains why it was not identified from the
363 forebrain-derived NSC datasets. Although there is no PRDM16 binding peak within the *Wnt3a*
364 locus in the CUT&TAG data from NSCs, there is a peak in the intronic region of *Wnt3a* in the
365 data from the dorsal midline tissue (**Supplementary Fig.5C**). This suggests that it may also
366 be regulated by PRDM16. We thus examined the scRNA-seq data (La Manno et al., 2021) and
367 confirmed that multiple components in the Wnt and BMP pathways are present in the CH and
368 ChP clusters (**Supplementary Fig.5D**). To systematically measure expression changes of Wnt
369 and BMP signaling components in the *Prdm16* mutant brain, we applied a multiplexed
370 fluorescent *in situ* approach, Single-Cell Resolution in Situ Hybridization On Tissues
371 (SCRINSHOT) (Sountoulidis et al., 2020). In this method each mRNA molecule is hybridized
372 with three gene-specific padlock probes, amplified by rolling cycle amplification and then
373 visualized by florescent dye-conjugated detection probes. A dot of fluorescent signal
374 corresponds to one mRNA molecule. Thus, the number of dots in each cell correlates with the
375 level of mRNA expression for each gene, allowing quantitative measurement of gene
376 expression in single cell resolution.

377 We designed probes for ten Wnt and five BMP pathway components (**Fig. 7**). Additionally, we
378 included probes for the ChP marker gene *Ttr* and *Foxj1*, the neural progenitor markers *Sox2*,
379 *Hes5* and *Zbtb20,* as well as the neuronal marker Ngn2. To minimize technical variation, we
380 performed SCRINSHOT in pairs of control and *Prdm16* mutant brains, with each pair being
381 processed in the same reaction chamber throughout the hybridization procedure.

382 In the control brain, *Ttr* and Foxj1 are highly expressed in the ChP epithelium at E11.5 and
383 E12.5, and several Wnt (*Wnt2b*, *Wnt7b*, *Wnt5a*, *Wnt3a*, *Fzd10* and *Axin2*) and BMP
384 components (*BMP4* and *BMP7*) display certain tissue specificity: the Wnt genes are more
385 enriched at CH while the BMP genes are more at the ChP. A few representative images from
386 E11.5 samples are presented in **Fig. 7 A-B**. Except *Wnt2b*, *Wnt* genes also show relatively low
387 expression in the ChP cells, consistent with the notion that Wnt signaling is present and required
388 at the ChP (Parichha et al., 2022).

389 Next, we intended to quantify expression changes of these genes in *Prdm16* mutant CH and
390 ChP cells. As the expression of *Wnt2b* was relatively unchanged in the mutant (**Supplementary**
391 **Fig. 1** and **Fig. 7A**), we used *Wnt2b*-expressing cells to define the CH cells and those expressing
392 *Ttr* to define ChP cells in the wild-type brain slice. There were about 110 cells in each region
393 of one brain slice. Because the mutant slice showed little *Ttr* signal, we only used the *Wnt2b*-
394 expressing cells at the most anterior side as the boarder and included 110 cells under the boarder
395 as the CH cells, and the further 110 cells as the mutant ChP cells, as shown in the images with
396 DAPI and cell outlines (**Fig. 7A and 7D**). We then measured the dot count of each gene in these
397 220 cells in each sample and summarized the changes calculated from three pairs of animals in
398 the violin plots (**Fig. 7 C** and **Supplementary Fig. 6A**). Expression of *Ttr* and *Foxj1* is severely
399 reduced, while *Sox2*, *Hes5* and *Ngn2* all become upregulated in the mutant ChP, indicating a
400 fate transformation of ChP epithelial to neural cells. This fully agrees with our immunostaining
401 and conventional *in situ* results (**Fig. 1** and **Supplementary Fig. 1**). Similar to BMP4, other
402 BMP components we tested including *BMP7*, *Smad6*, *Smad7 and Nog* are unchanged. As
403 *Smad6* and *Smad7* are not only inhibitory factors of BMP signaling but also downstream targets,
404 this result suggests that BMP signaling is generally normal in the *Prdm16* mutant.

405 Remarkably, *Wnt3a* and *Wnt7b* are significantly upregulated in the mutant ChP (**Fig. 7B-E** and
406 **Supplementary Fig. 6A-C**). The Wnt target gene *Axin2* is also upregulated, indicating that the
407 activity of Wnt signaling is aberrantly elevated in the *Prdm16* mutant ChP. Thus, the normal
408 function of *Prdm16* represses WNT signaling in the developing ChP.

409 **Levels of Wnt activity correlate with cell proliferation in the developing ChP and CH**

410 As *Prdm16* mutant ChP cells showed elevated Wnt signaling (**Fig. 7 A-C**) and ectopic cell
411 proliferation (**Fig. 2**), we assessed the relationship between Wnt signaling and cell proliferation
412 in the ChP and CH at E12.5. We defined cell proliferation state using expression levels of

413 *mKi67* by quantifying the number of dots of *mKi67* SCRINSHOT signal in 110 CH and 110
414 ChP cells in each wild-type and mutant sample. There is a significant increase of *mKi67*
415 expression in *Prdm16* mutant ChP cells at E12.5 (**Fig. 7F**), accompanied by significantly
416 increased *Wnt3a*, *Wnt7b* and *Axin2* levels (**Fig. 7F** and **Supplementary Fig 6B-C**). In contrast,
417 there is little or no increase of *mKi67* signal in the mutant CH, suggesting that the effect of
418 PRDM16 is mainly cell-autonomous. We then performed linear regression and Pearson
419 correlation analyses to see correlations between ChP markers, BMP and Wnt genes.
420 Interestingly, the level of *Axin2* best correlates the level of m*Ki67*, even better than that with
421 other Wnt genes in both wild-type ($r = 0.46$; $p < 2.2$ E-35) and mutant ($r= 0.56$; $p < 1.6$ E-55)
422 CH and ChP cells **(Fig. 7G** and **Supplementary Fig. 6D**). This result suggests that Wnt activity
423 is responsible for cell proliferation in the CH and ChP region. In line with this finding, it was
424 shown that ectopic Wnt signaling converts ChP cells into proliferative CH neural cells
425 (Parichha et al., 2022).

426 Similarly, in the 4th ventricle, *Prdm16* deletion caused severe ChP defects (**Fig. 1D** and
427 **Supplementary Fig. 7**). In this region from wild-type brains, *Wnt7b* showed little expression,
428 while *Wnt3a* and *Wnt1* appeared abundant in the two sides that flanking the hChP. Interestingly,
429 these two genes and *mKi67* all became ectopically expressed in *Prdm16* mutant ChP cells. Thus,
430 PRDM16 also suppresses Wnt signaling in the hindbrain ChP. Taken together, our results
431 suggest that specification of the ChP epithelium requires a process transitioning proliferating
432 NSCs into quiescence, and that this process is mediated by a suppressive role of PRDM16 on
433 Wnt signaling.

434

435

436

437

438

439

440

441 **Discussion**

442 Combinatory activities of morphogens are exploited throughout animal development and tissue
443 homeostasis. It remains to be determined how the right combination and levels of these
444 molecules are controlled in each specific setting. In this study we reveal that PRDM16
445 collaborates with BMP signaling to regulate cell quiescence, a prerequisite for ChP epithelial
446 cell specification. We show that BMP signaling up-regulates expression of PRDM16 whose
447 activity facilitates the regulatory activity of SMAD transcription factors to suppress expression
448 of the Wnt genes. Using SCRINSHOT that allows us to fine dissect gene expression change,
449 we find that expression of the genes encoding morphogens is under complex regulation, as
450 distinct Wnt ligand genes are differentially regulated even in the same tissue. In the case of ChP
451 specification, *Wnt7b* and *Wnt3a* were sensitive to *Prdm16* deletion in the forebrain, while *Wnt1*
452 and *Wnt3a* showed dramatic change in the hindbrain.

453 Wnt and BMP signaling pathways are integrated in many biological processes (Itasaki and
454 Hoppler, 2010). The crosstalk between BMP and WNT signaling is complex as it can be
455 synergistic or antagonistic. Surprisingly, both types of effects exist in the specification of ChP
456 epithelium. Here BMP signaling induces NSC quiescence, as evidenced by the presence of
457 ectopic proliferating cells at the ChP in *Bmpr1a* mutant mice (Hebert et al., 2002), while Wnt
458 signaling promotes proliferation since the gain-of-function condition of beta-Catenin
459 phenocopies *Bmpr1a* mutant animals (Parichha et al., 2022). On the other hand, adding a low
460 dose of Wnt activator to cell culture medium enhances programing efficiency of ChP epithelial
461 cells induced by BMP4 (Pellegrini et al., 2020), and loss-of-function of beta-Catenin resulted
462 in under-developed ChP structure (Parichha et al., 2022), suggesting that BMP and WNT
463 signaling collaborate to promote ChP epithelial cell differentiation. Our work demonstrated that
464 PRDM16 ensures the right balance of BMP and Wnt activity by maintaining a low level of Wnt
465 gene expression in the developing ChP.

466 Moreover, we showed that at the molecular level, PRDM16 functions as a co-repressor for the
467 SMAD4/pSMAD1/5/8 complex. PRDM16 was shown to physically interact with SMAD3 in
468 *in vitro* assays (Warner et al., 2007) and antagonize TGF-β induced cell cycle arrest (Takahata
469 et al., 2009). However, we tried hard to detect a stable PRDM16/SMAD4/pSMAD1/5/8
470 complex in co-immunoprecipitation experiments but never succeeded (data not shown). Instead,
471 we found that PRDM16 and SMAD4 bind to the same DNA molecule in the sequential ChIP
472 assay, suggesting that the cooperative activity of SMAD4 and PRDM16 occurs at their co-

473 bound *cis* regulatory elements. Remarkably, we identified the intrinsic difference of the DNA
474 motifs bound by SMADs when associated with PRDM16 compared to those without PRDM16,
475 with SMADs preferentially binding to the palindromic motif in the presence of PRDM16 and
476 to the classic GC-rich SBE motifs in the absence of PRDM16. This provides a mechanistic
477 insight into how SMADs switch its regulatory activity from repressing to activating gene
478 expression. In contrast to the previous report indicating that PRDM16 antagonized the anti-
479 proliferation activity of TGF-β and SMAD3, we show here that PRDM16 collaborates SMAD4
480 and pSMAD1/5/8 to suppress proliferation genes, which is consistent with the quiescence-
481 inducing function of BMP signaling. Moreover, while it was reported that PRDM16 promotes
482 Wnt signaling by stabilizing nuclear beta-Catenin in the craniofacial tissue (Shull et al., 2022),
483 we detected the opposite outcome in the ChP and cultured NSCs, with ectopic WNT gene
484 expression in the absence of *Prdm16*, suggesting that PRDM16 represses Wnt genes in these
485 contexts. Notably, PRDM16, Wnt and BMP co-exist in various developmental settings, such
486 as craniofacial development (Bjork et al., 2010; Nie et al., 2006; Shull et al., 2022), heart
487 formation (Arndt et al., 2013; Gessert and Kuhl, 2010; van Wijk et al., 2007), limb patterning
488 (Bjork et al., 2010; Geetha-Loganathan et al., 2008; Robert, 2007), adult intestinal stem cells
489 (He et al., 2004; Korinek et al., 1998; Stine et al., 2019) *etc*. We speculate a similar regulatory
490 circuit is used in some, if not all, of these settings.

491 ChPe epithelial cells derive from proliferating NSCs, without intermediate fate-commitment
492 steps. This property endows ChP cells with higher plasticity and makes them more vulnerable
493 to abnormal genetic and cellular change, to which high occurrence frequency of ChP tumors in
494 fetuses and young children may be attributed (Wolff et al., 2002). As an essential brain structure,
495 the ChP releases cerebrospinal fluid (CSF) and acts as a brain-blood barrier (Johansson, 2014;
496 Lehtinen et al., 2013; Lun et al., 2015). Its dysfunction has been linked with several types of
497 human diseases including hydrocephalus, Alzheimer's disease, multiple sclerosis (Lun et al.,
498 2015). Deepening our knowledge on the development of ChP will provide new insights into
499 potential therapeutics to prevent or treat ChP tumors and other ChP-related diseases.

500

501

502

503 **Materials and methods**

504 **Animals**

505 All animal procedures were approved by Swedish agriculture board (Jordbruks Verket) with
506 document number Dnr 11553-2017 and 11766-2022. The *Prdm16*^{cGT} mice (Strassman et al.,
507 2017) were maintained by outcrossing with the FVB/NJ line.

508 **In situ hybridization**:

509 To make probes for conventional RNA in situ hybridization, genomic regions covering one
510 exon or full-length cDNA were PCR amplified to generate fragments with restriction enzyme
511 overhangs. The sequences of all oligos were included in Supplementary table 1. The fragments
512 were inserted to the pBluescript SK(II) vector. In vitro transcription was performed as
513 previously described (He et al., 2021). The mouse brains at defined ages were dissected and
514 fixed for 12 hours in 4% PFA, dehydrated in 25% sucrose, cryoprotected and embedded in
515 O.C.T. The brain samples were then sectioned at 18 μm thickness on Leica cryostats CM3050s.
516 RNA *in situ* hybridization was performed using digoxigenin-labeled riboprobes as described
517 previously. Detailed protocols are available upon request. Images were taken using a Leica
518 DMLB microscope.

519 **Immunostaining**

520 Immunostaining was done according to standard protocols as previously used (Dai et al., 2013a).
521 For EdU labeling, EdU (5-ethynyl-2′-deoxyuridine) (5-20 μg/g of body weight) was injected
522 into the peritoneal cavity of pregnant mice. EdU incorporation was detected with the Click-iT
523 assay (Invitrogen) according to the manufacturer's instructions. Imaging was done on Zeiss
524 confocal microscope. ZEN (ZeissLSM800), ImageJ (NIH) and Photoshop (Adobe) were used
525 for analysis and quantification.

526 **NSC culture**

527 Control and mutant embryonic cortices from E13.5 animals were dissected and dissociated into
528 single cell suspension and digested with Acutase (Sigma). Cells were maintained in
529 proliferation media (STEMCELL Technologies). Lentivirus expressing Flag-Prdm16 and a
530 puromycin resistant gene in the pCDH vector was produced in 293-ft cells and used to infect a

531 wild-type NSC line derived from E13.5 forebrain, and the selected NSCs were maintained in
532 puromycin-containing medium for three passages before puromycin withdrawal.

533 **RT-qPCR**

534 *Prdm16_Expressing*, wild-type and mutant NSCs were cultured and treated with or without
535 BMP4 (Sigma). After 48-hour treatment, total RNAs were extracted using TRIzol reagent
536 (Invitrogen). Total RNA was further cleaned with Turbo DNase (Ambion) and used in reverse-
537 transcription with RT master mix (ThermoFisher). To ensure the absence of genomic DNA,
538 control qPCR was performed on the mock-reverse-transcribed RNA samples. The list of qPCR
539 primers is included in supplementary table 1.

540 **SCRINSHOT**

541 Brain sections were prepared in the same way as for regular *in situ* hybridization (described
542 above). The SCRINSHOT experiments were carried out according to the published method
543 (Sountoulidis et al., 2020). In brief, 3 padlock probes and 3 corresponding detection probes
544 were designed for each gene of interest. The slides with cryo-sectioned brain slices were
545 pretreated at 45˚C to reduce moisture and fixed in 4% PFA in 1X PBS, followed by washing in
546 PBS Tween-20 0.05% twice. Permeabilization of tissues were done by washing slides in 0.1M
547 HCl for 2mins 15s, followed by washing in PBS Tween-20 0.05% twice. Then a stepwise
548 dehydration was performed for the slides in 70%, 85% & 100% Ethanol and air. The SecureSeal
549 hybridization chamber (GRACE BIO-LABS, 621501) was then mounted to cover each pair of
550 control and *Prdm16* mutant brain slices. Samples were then blocked in a probe-free
551 hybridization reaction mixture of 1XAmplifase buffer (Lucigen, A1905B), 0.05M KCl, 20%
552 Formamide deionized (Millipore S4117), 0.1uM Oligo-dT, 0.1ug/ul BSA (New England
553 Biolabs, B9000S), 1U/ul RiboLock (Thermo, EO0384), and 0.2ug/ul tRNAs (Ambion,
554 AM7119). Then hybridization of padlock probes was done by incubating samples with padlock
555 probes (with the concentration of each one 0.01uM) mixed in blocking reagents used before
556 (no oligo dT used in this step). The slide was then put into a PCR machine to denature at 55˚C
557 for 15 minutes and hybridize at 45˚C for 120 minutes. Padlock probes were then ligated by
558 using SplintR ligase (NEB M0375) at 25˚C for 16 hours followed by RCA (rolling cycle
559 amplification) at 30˚C for 16 hours by using phi29 polymerase (Lucigen, 30221–2) and RCA
560 primer1. Then a fixation step was applied to stabilize RCA product in 4% PFA for 15 minutes
561 followed by washing in PBS Tween-20 0.05%. Then the hybridization of the first 3 genes was

562 done by mixing all 3 3' fluorophore-conjugated detection probes of each gene in reaction
563 reagent (2XSSC, 20% Formamide deionized, 0.1ug/ul BSA, and 0.5 ng/µl DAPI (Biolegend,
564 422801) followed by hybridization at 30˚C for 1 hour. The slides were washed in 20%
565 formamide in 2X SSC and then in 6X SSC, followed by dehydration in 70%, 85%, 100%
566 Ethanol until the chamber was removed. Then the samples were preserved in SlowFade Gold
567 Antifade mountnant (Thermo, S36936) and kept in dark before imaging. After image
568 acquisition, the first 3 detection probes were removed by using Uracil-DNA Glycosylase
569 (Thermo, EN0362), and the slides were ready for the next round of detection probe
570 hybridization. The procedure was repeated until all genes were hybridized and imaged.

571 Images were acquired with Zeiss Axio Observer 7 fluorescent microscope with an automated
572 stage setting to fix imaging region for different hybridization rounds. Image analysis was done
573 according to the published method (Sountoulidis et al., 2020). In brief, the DAPI channel from
574 each round was extracted to measure the shift of imaging. The images were then aligned for all
575 gene channels in Zen by Creating Image Subset with the shifting value. After alignment, images
576 were exported into TIFF files and the threshold analysis was carried out for individual channel
577 one by one in CellProfiler with scripts provided by the published method (Alexandros et al.
578 2020). Then nuclear segmentation was done manually in Fiji ROI manager to obtain nuclear
579 ROIs, followed by an expansion of 2 um in CellProfiler to obtain cell ROIs. Then signal dots
580 were count in these cell ROIs for each gene in CellProfiler and Fiji. Summary of the dot counts
581 for each gene was exported to Excel files.

582 **CUT&TAG**

583 CUT&TAG was performed according to the published method (Kaya-Okur et al., 2019). In
584 brief, *Prdm16*_E and *Prdm16* mutant NSCs were cultured in NeuroCult™ Proliferation Kit
585 (Stem cell technologies, 05702) for 3 days with or without BMP4 at concentration of 25ng/ml
586 medium (Sigma, H4916). Cells on day 3 were then shortly rinsed with 1X PBS and resuspended
587 in 1ml cold NE1 buffer on ice. Nuclei were lightly fixed with 0.1% formaldehyde to 1ml PBS
588 at RT for 2 minutes and neutralized with 75mM Glycine. Nuclei were then washed for 3 times,
589 resuspended in 1mL wash buffer and mixed with 90uL Concanavalin A-coated magnetic beads
590 (Polyscience 86057). The nuclei/beads mix was then blocked with 800 uL cold Antibody buffer
591 for 5 minutes and resuspended in 1.2 mL Antibody buffer and aliquoted into 8 tubes with 150
592 uL each. 2 uL Anti-PRDM16 (Generous gift from Bryan Bjork lab) or IgG (SIGMA-ALDRICH,
593 I5006) was added into each tube for an overnight incubation at 4°C. The beads/nuclei/antibody

594 mix was then washed with Dig-wash buffer and incubated with secondary antibody (1:100
595 dilution) for 1 hour. After further washes with the Dig-wash buffer. a pA-Tn5 adaptor complex
596 in Dig-300 buffer was added to the beads for 1 hour reaction. The beads were then washed with
597 Dig-300 buffer before the incubation with 300ul Tagmentation buffer at 37°C for 1 hour. Then
598 10ul 0.5M EDTA, 3uL 10% SDS and 2.5uL 20 mg/mL proteinase K (Invitrogen) were used to
599 stop the reaction. Then the resultant DNA was purified with DNA clean & Concentrator kit
600 (ZYMO Research D4013) and eluted in 25uL Elution buffer. To generate libraries, 21uL
601 fragment DNA was mixed with 2uL 10uM Universal i5 primer, 2uL 10uM uniquely barcoded
602 i7 primer and 25uL PCR master mix (NEB Phusion® High-Fidelity PCR Master Mix with HF
603 Buffer, M0531). The PCR condition was as follows: 72°C 5min, 98°C 30s, repeat 12 times
604 (98°C 10s, 63°C 10s), 72°C 1 min and hold 4°C. The libraries were cleaned with standard
605 Ampure XP beads as previously described. Libraries from four biological replicates were
606 produced for each condition.

607 **ChIP**

608 ChIP was performed as previously described (Dai et al., 2013b). For each ChIP reaction, 10
609 million Prdm16_E, Prdm16_KO NSCs with or without 3-day BMP4 treatment were fixed,
610 lysed and made into chromatin extract. 2ug SMAD4 (Proteintech, 10231-1-AP), 2ug
611 pSMAD1/5/8 (Millipore, AB3848-1), 2ug SMAD3 (abcam, ab227223) and 2 ug c-FOS
612 antibodies (Invitrogen, MA5-15055) were used in each ChIP reaction. The same chromatin
613 lysate was used for sequential ChIP but with more antibodies in each reaction: 5 ug of IgG or
614 the PRDM16 antibody in the first round of immunoprecipitation. The elutes were then
615 precleared again using gamma-bind G beads, divided into two equal halves and
616 immunoprecipitated with 2 ug of IgG or the SMAD4 antibody. The precipitated DNA was
617 reverse cross-linked, and then purified using the Qiagen PCR purification kit.

618 **Computation analyses**

619 **ChIP-seq libraries and analyses.** 0.2% input and ChIPed DNA were made into libraries using
620 the NEBNext Ultra™ II DNA Library Prep Kit and sequenced on the Illumina Nextseq500
621 platform. Three replicates of ChIP-seq samples, after the adaptor trimming by Trimmomatic,
622 were mapped to the UCSC *Mus musculus* (mm10) genome assembly using Bowtie2 with the
623 default parameters. The uniquely mapped reads (with mapping quality >= 20) were used for
624 further analyses. The peaks were called by HOMER (v4.10) (Heinz et al., 2010). The

625 reproducibility between replicates was estimated by Irreproducibility Discovery Rate (IDR),
626 using the HOMER IDR pipeline (https://github.com/karmel/homer-idr). As suggested by the
627 Encode IDR guideline, we used a relatively relaxed parameter "-F 2 -fdr 0.3 -P .1 -L 3 -LP .1"
628 for the true/pseudo/pooled replicates by the HOMER peak calling. The final confident peaks
629 were determined by an IDR < 5%. The peaks that were overlapped with mm10 blacklist were
630 also removed.

631 **CUT&TAG analyses.** The CUT&TAG samples of Prdm16_E and Prdm16 mutant NSCs in
632 four replicates, and of Prdm16 from CH and ChP area at stage 12.5 embryos in three replicates,
633 were mapped to mm10 genome assembly using Bowtie2 (bowtie2 --end-to-end --very-sensitive
634 --no-mixed --no-discordant --phred33 -I 10 -X 700). The CUT&TAG coverage for these
635 samples were generated by bedtools genomeCoverageBed and normalized to the library depths
636 to give a read per million per base (RPM). By using the peak caller SEACR (Meers et al., 2019),
637 which was designed for calling peaks from sparse chromatin profiling data such as CUT&TAG
638 [22], we performed peak calling with FDR < 10% for each replicated sample (SEACR_1.3.sh
639 normalized_coverage 0.1 non stringent output_peaks). To identify confident peaks, we selected
640 the common peaks, which were called from all replicates for each condition. Peak overlapping
641 analysis was performed by Homer mergePeaks function with default parameters. *De novo* motif
642 discovery from SMAD4 and pSMAD1/5/8 peaks in Prdm16_E NSCs and Prdm16 mutant NSCs
643 were performed by MEME-ChIP software (Machanick and Bailey, 2011) (parameters: -ccut
644 100 -meme-p 5 -dna -meme-mod anr -minw 5 -maxw 15 -filter-thresh 0.05).

645 The CUT&TAG samples of H3K4me3 BMP4-treated and non-treated Prdm16_E and
646 Prdm16_KO cells in 2 or 3 replicates were mapped to mm10 genome assembly using Bowtie2
647 (bowtie2 --end-to-end --very-sensitive --no-mixed --no-discordant --phred33 -I 10 -X 700).
648 Differential analysis of TSS up-stream and down-stream 500 bp between Prdm16_E BMP-
649 treated vs non-BMP-treated and Prdm16_KO vs Prdm16_E BMP-treated were performed by
650 Limma R package (Ritchie et al., 2015). Gene Ontology (GO) enrichment analysis of up-
651 regulated and down-regulated regions was performed by PANTHER (Thomas et al., 2022).

652 **scRNA-seq analyses.** The scRNA-seq data of the developing mouse brain were obtained from
653 (La Manno et al., 2021). The counts per cell were normalized by logNormCounts function in
654 Bioconductor package "scater" and the normalized expression data per cell were used to
655 generate gene expression violin plots. To test whether Prdm16 target gene sets of Prdm16 with
656 and without BMP4 and ChP E12.5 are significantly enriched among the scRNA-seq gene mean

expression in each identified cell type cluster, the gene set enrichment analysis (GESA) "fgesa" Bioconductor package was used [ref: Korotkevich G. et al. Fast gene set enrichment analysis. bioRxiv, 2021. http://biorxiv.org/content/early/2016/06/20/060012].

Acknowledgements

We thank the animal experimental core facility and the imaging facility of Stockholm University and Bioinformatics and Expression analysis core facility at Karolinska Institute, Sweden, for their service and support. We thank Christos Samakovlis and his lab members for technical help on SCRINSHOT experiments. We also appreciate technical help from Adrian Martinez Martin, financial support by the Australian Research Council (ARC) Future Fellowship (FT160100143) and ANU Future Scheme to J. W. The project was supported by the research project grant from Swedish Research Council (Vetenskapsrådet, 2020-03543) and the research grants from Swedish Cancerfonden (CAN 2017/529 and 20 1046 PjF 01 H) to Q.D.

Author contributions

Q.D. conceived and designed the project. L.H. performed all of the experiments. J.W performed all computational analysis. Q.D., J.W. and L.H. analysed and interpreted the data. Q.D. wrote the manuscript with input from L.H. and J.W.

682 **Reference:**

683 Aguilo, F., Avagyan, S., Labar, A., Sevilla, A., Lee, D.F., Kumar, P., Lemischka, I.R., Zhou, B.Y.,
684 and Snoeck, H.W. (2011). Prdm16 is a physiologic regulator of hematopoietic stem cells.
685 Blood *117*, 5057-5066.
686 al, A.P.e. (2020). Canonical Wnt signaling exerts bidirectional control on choroid plexus
687 epithelial development. BIORXIV.
688 Arndt, A.K., Schafer, S., Drenckhahn, J.D., Sabeh, M.K., Plovie, E.R., Caliebe, A., Klopocki, E.,
689 Musso, G., Werdich, A.A., Kalwa, H.*, et al.* (2013). Fine mapping of the 1p36 deletion
690 syndrome identifies mutation of PRDM16 as a cause of cardiomyopathy. Am J Hum Genet
691 *93*, 67-77.
692 Baizabal, J.M., Mistry, M., Garcia, M.T., Gomez, N., Olukoya, O., Tran, D., Johnson, M.B.,
693 Walsh, C.A., and Harwell, C.C. (2018). The Epigenetic State of PRDM16-Regulated Enhancers
694 in Radial Glia Controls Cortical Neuron Position. Neuron *98*, 945-962 e948.
695 Benayoun, B.A., Pollina, E.A., Ucar, D., Mahmoudi, S., Karra, K., Wong, E.D., Devarajan, K.,
696 Daugherty, A.C., Kundaje, A.B., Mancini, E.*, et al.* (2014). H3K4me3 breadth is linked to cell
697 identity and transcriptional consistency. Cell *158*, 673-688.
698 Bjork, B.C., Turbe-Doan, A., Prysak, M., Herron, B.J., and Beier, D.R. (2010). Prdm16 is
699 required for normal palatogenesis in mice. Hum Mol Genet *19*, 774-789.
700 Chui, A., Zhang, Q., Dai, Q., and Shi, S.H. (2020). Oxidative stress regulates progenitor
701 behavior and cortical neurogenesis. Development *147*.
702 Chuikov, S., Levi, B.P., Smith, M.L., and Morrison, S.J. (2010). Prdm16 promotes stem cell
703 maintenance in multiple tissues, partly by regulating oxidative stress. Nat Cell Biol *12*, 999-
704 1006.
705 Dai, Q., Andreu-Agullo, C., Insolera, R., Wong, L.C., Shi, S.H., and Lai, E.C. (2013a). BEND6 is a
706 nuclear antagonist of Notch signaling during self-renewal of neural stem cells. Development
707 *140*, 1892-1902.
708 Dai, Q., Ren, A., Westholm, J.O., Serganov, A.A., Patel, D.J., and Lai, E.C. (2013b). The BEN
709 domain is a novel sequence-specific DNA-binding domain conserved in neural transcriptional
710 repressors. Genes Dev *27*, 602-614.
711 Dennler, S., Itoh, S., Vivien, D., ten Dijke, P., Huet, S., and Gauthier, J.M. (1998). Direct
712 binding of Smad3 and Smad4 to critical TGF beta-inducible elements in the promoter of
713 human plasminogen activator inhibitor-type 1 gene. The EMBO journal *17*, 3091-3100.
714 Gao, S., Steffen, J., and Laughon, A. (2005). Dpp-responsive silencers are bound by a trimeric
715 Mad-Medea complex. J Biol Chem *280*, 36158-36164.
716 Geetha-Loganathan, P., Nimmagadda, S., and Scaal, M. (2008). Wnt signaling in limb
717 organogenesis. Organogenesis *4*, 109-115.
718 Gessert, S., and Kuhl, M. (2010). The multiple phases and faces of wnt signaling during
719 cardiac differentiation and development. Circ Res *107*, 186-199.
720 Harrison-Uy, S.J., and Pleasure, S.J. (2012). Wnt signaling and forebrain development. Cold
721 Spring Harb Perspect Biol *4*, a008094.
722 He, L., Jones, J., He, W., Bjork, B.C., Wen, J., and Dai, Q. (2021). PRDM16 regulates a
723 temporal transcriptional program to promote progression of cortical neural progenitors.
724 Development *148*.
725 He, X.C., Zhang, J., Tong, W.G., Tawfik, O., Ross, J., Scoville, D.H., Tian, Q., Zeng, X., He, X.,
726 Wiedemann, L.M.*, et al.* (2004). BMP signaling inhibits intestinal stem cell self-renewal
727 through suppression of Wnt-beta-catenin signaling. Nat Genet *36*, 1117-1121.

728 Hebert, J.M., Mishina, Y., and McConnell, S.K. (2002). BMP signaling is required locally to
729 pattern the dorsal telencephalic midline. Neuron *35*, 1029-1041.
730 Heinz, S., Benner, C., Spann, N., Bertolino, E., Lin, Y.C., Laslo, P., Cheng, J.X., Murre, C., Singh,
731 H., and Glass, C.K. (2010). Simple combinations of lineage-determining transcription factors
732 prime cis-regulatory elements required for macrophage and B cell identities. Mol Cell *38*,
733 576-589.
734 Hill, C.S. (2016). Transcriptional Control by the SMADs. Cold Spring Harb Perspect Biol *8*.
735 Horvath, C., and Scheele, C. (2022). PRDM16 stability and metabolically healthy adipose
736 tissue. Nat Metab *4*, 1095-1096.
737 Inoue, M., Iwai, R., Tabata, H., Konno, D., Komabayashi-Suzuki, M., Watanabe, C., Iwanari,
738 H., Mochizuki, Y., Hamakubo, T., Matsuzaki, F.*, et al.* (2017). Prdm16 is crucial for
739 progression of the multipolar phase during neural differentiation of the developing
740 neocortex. Development *144*, 385-399.
741 Itasaki, N., and Hoppler, S. (2010). Crosstalk between Wnt and bone morphogenic protein
742 signaling: a turbulent relationship. Dev Dyn *239*, 16-33.
743 Johansson, P.A. (2014). The choroid plexuses and their impact on developmental
744 neurogenesis. Front Neurosci *8*, 340.
745 Kajimura, S., Seale, P., Tomaru, T., Erdjument-Bromage, H., Cooper, M.P., Ruas, J.L., Chin, S.,
746 Tempst, P., Lazar, M.A., and Spiegelman, B.M. (2008). Regulation of the brown and white fat
747 gene programs through a PRDM16/CtBP transcriptional complex. Genes Dev *22*, 1397-1409.
748 Kalani, M.Y., Cheshier, S.H., Cord, B.J., Bababeygy, S.R., Vogel, H., Weissman, I.L., Palmer,
749 T.D., and Nusse, R. (2008). Wnt-mediated self-renewal of neural stem/progenitor cells. Proc
750 Natl Acad Sci U S A *105*, 16970-16975.
751 Katada, S., Takouda, J., Nakagawa, T., Honda, M., Igarashi, K., Imamura, T., Ohkawa, Y., Sato,
752 S., Kurumizaka, H., and Nakashima, K. (2021). Neural stem/precursor cells dynamically
753 change their epigenetic landscape to differentially respond to BMP signaling for fate
754 switching during brain development. Genes Dev *35*, 1431-1444.
755 Kaya-Okur, H.S., Wu, S.J., Codomo, C.A., Pledger, E.S., Bryson, T.D., Henikoff, J.G., Ahmad, K.,
756 and Henikoff, S. (2019). CUT&Tag for efficient epigenomic profiling of small samples and
757 single cells. Nat Commun *10*, 1930.
758 Korinek, V., Barker, N., Moerer, P., van Donselaar, E., Huls, G., Peters, P.J., and Clevers, H.
759 (1998). Depletion of epithelial stem-cell compartments in the small intestine of mice lacking
760 Tcf-4. Nat Genet *19*, 379-383.
761 La Manno, G., Siletti, K., Furlan, A., Gyllborg, D., Vinsland, E., Mossi Albiach, A., Mattsson
762 Langseth, C., Khven, I., Lederer, A.R., Dratva, L.M.*, et al.* (2021). Molecular architecture of
763 the developing mouse brain. Nature *596*, 92-96.
764 Lehtinen, M.K., Bjornsson, C.S., Dymecki, S.M., Gilbertson, R.J., Holtzman, D.M., and Monuki,
765 E.S. (2013). The choroid plexus and cerebrospinal fluid: emerging roles in development,
766 disease, and therapy. J Neurosci *33*, 17553-17559.
767 Liddelow, S.A., Dziegielewska, K.M., Vandeberg, J.L., and Saunders, N.R. (2010).
768 Development of the lateral ventricular choroid plexus in a marsupial, Monodelphis
769 domestica. Cerebrospinal Fluid Res *7*, 16.
770 Lun, M.P., Monuki, E.S., and Lehtinen, M.K. (2015). Development and functions of the
771 choroid plexus-cerebrospinal fluid system. Nat Rev Neurosci *16*, 445-457.
772 Machanick, P., and Bailey, T.L. (2011). MEME-ChIP: motif analysis of large DNA datasets.
773 Bioinformatics *27*, 1696-1697.

774 Meers, M.P., Tenenbaum, D., and Henikoff, S. (2019). Peak calling by Sparse Enrichment
775 Analysis for CUT&RUN chromatin profiling. Epigenetics Chromatin *12*, 42.
776 Mira, H., Andreu, Z., Suh, H., Lie, D.C., Jessberger, S., Consiglio, A., San Emeterio, J.,
777 Hortiguela, R., Marques-Torrejon, M.A., Nakashima, K.*, et al.* (2010). Signaling through
778 BMPR-IA regulates quiescence and long-term activity of neural stem cells in the adult
779 hippocampus. Cell stem cell *7*, 78-89.
780 Nie, X., Luukko, K., and Kettunen, P. (2006). BMP signalling in craniofacial development. Int J
781 Dev Biol *50*, 511-521.
782 Parichha, A., Suresh, V., Chatterjee, M., Kshirsagar, A., Ben-Reuven, L., Olender, T., Taketo,
783 M.M., Radosevic, V., Bobic-Rasonja, M., Trnski, S.*, et al.* (2022). Constitutive activation of
784 canonical Wnt signaling disrupts choroid plexus epithelial fate. Nat Commun *13*, 633.
785 Pellegrini, L., Bonfio, C., Chadwick, J., Begum, F., Skehel, M., and Lancaster, M.A. (2020).
786 Human CNS barrier-forming organoids with cerebrospinal fluid production. Science *369*.
787 Pliner, H.A., Packer, J.S., McFaline-Figueroa, J.L., Cusanovich, D.A., Daza, R.M., Aghamirzaie,
788 D., Srivatsan, S., Qiu, X., Jackson, D., Minkina, A.*, et al.* (2018). Cicero Predicts cis-Regulatory
789 DNA Interactions from Single-Cell Chromatin Accessibility Data. Mol Cell *71*, 858-871 e858.
790 Pyrowolakis, G., Hartmann, B., Muller, B., Basler, K., and Affolter, M. (2004). A simple
791 molecular complex mediates widespread BMP-induced repression during Drosophila
792 development. Dev Cell *7*, 229-240.
793 Rhodes, C.T., Thompson, J.J., Mitra, A., Asokumar, D., Lee, D.R., Lee, D.J., Zhang, Y., Jason, E.,
794 Dale, R.K., Rocha, P.P.*, et al.* (2022). An epigenome atlas of neural progenitors within the
795 embryonic mouse forebrain. Nat Commun *13*, 4196.
796 Ritchie, M.E., Phipson, B., Wu, D., Hu, Y., Law, C.W., Shi, W., and Smyth, G.K. (2015). limma
797 powers differential expression analyses for RNA-sequencing and microarray studies. Nucleic
798 Acids Res *43*, e47.
799 Robert, B. (2007). Bone morphogenetic protein signaling in limb outgrowth and patterning.
800 Dev Growth Differ *49*, 455-468.
801 Shimada, I.S., Acar, M., Burgess, R.J., Zhao, Z., and Morrison, S.J. (2017). Prdm16 is required
802 for the maintenance of neural stem cells in the postnatal forebrain and their differentiation
803 into ependymal cells. Genes Dev *31*, 1134-1146.
804 Shull, L.C., Lencer, E.S., Kim, H.M., Goyama, S., Kurokawa, M., Costello, J.C., Jones, K., and
805 Artinger, K.B. (2022). PRDM paralogs antagonistically balance Wnt/beta-catenin activity
806 during craniofacial chondrocyte differentiation. Development *149*.
807 Sountoulidis, A., Liontos, A., Nguyen, H.P., Firsova, A.B., Fysikopoulos, A., Qian, X., Seeger,
808 W., Sundstrom, E., Nilsson, M., and Samakovlis, C. (2020). SCRINSHOT enables spatial
809 mapping of cell states in tissue sections with single-cell resolution. PLoS Biol *18*, e3000675.
810 Stine, R.R., Sakers, A.P., TeSlaa, T., Kissig, M., Stine, Z.E., Kwon, C.W., Cheng, L., Lim, H.W.,
811 Kaestner, K.H., Rabinowitz, J.D.*, et al.* (2019). PRDM16 Maintains Homeostasis of the
812 Intestinal Epithelium by Controlling Region-Specific Metabolism. Cell stem cell *25*, 830-845
813 e838.
814 Strassman, A., Schnutgen, F., Dai, Q., Jones, J.C., Gomez, A.C., Pitstick, L., Holton, N.E.,
815 Moskal, R., Leslie, E.R., von Melchner, H.*, et al.* (2017). Generation of a multipurpose Prdm16
816 mouse allele by targeted gene trapping. Dis Model Mech *10*, 909-922.
817 Takahata, M., Inoue, Y., Tsuda, H., Imoto, I., Koinuma, D., Hayashi, M., Ichikura, T., Yamori,
818 T., Nagasaki, K., Yoshida, M.*, et al.* (2009). SKI and MEL1 cooperate to inhibit transforming
819 growth factor-beta signal in gastric cancer cells. J Biol Chem *284*, 3334-3344.

820 Thomas, P.D., Ebert, D., Muruganujan, A., Mushayahama, T., Albou, L.P., and Mi, H. (2022).
821 PANTHER: Making genome-scale phylogenetics accessible to all. Protein Sci *31*, 8-22.
822 van Wijk, B., Moorman, A.F., and van den Hoff, M.J. (2007). Role of bone morphogenetic
823 proteins in cardiac differentiation. Cardiovasc Res *74*, 244-255.
824 Wang, Q., Li, H., Tajima, K., Verkerke, A.R.P., Taxin, Z.H., Hou, Z., Cole, J.B., Li, F., Wong, J.,
825 Abe, I.*, et al.* (2022). Post-translational control of beige fat biogenesis by PRDM16
826 stabilization. Nature *609*, 151-158.
827 Warner, D.R., Horn, K.H., Mudd, L., Webb, C.L., Greene, R.M., and Pisano, M.M. (2007).
828 PRDM16/MEL1: a novel Smad binding protein expressed in murine embryonic orofacial
829 tissue. Biochim Biophys Acta *1773*, 814-820.
830 Watanabe, M., Kang, Y.J., Davies, L.M., Meghpara, S., Lau, K., Chung, C.Y., Kathiriya, J.,
831 Hadjantonakis, A.K., and Monuki, E.S. (2012). BMP4 sufficiency to induce choroid plexus
832 epithelial fate from embryonic stem cell-derived neuroepithelial progenitors. J Neurosci *32*,
833 15934-15945.
834 Weiss, A., Charbonnier, E., Ellertsdottir, E., Tsirigos, A., Wolf, C., Schuh, R., Pyrowolakis, G.,
835 and Affolter, M. (2010). A conserved activation element in BMP signaling during Drosophila
836 development. Nat Struct Mol Biol *17*, 69-76.
837 Wolff, J.E., Sajedi, M., Brant, R., Coppes, M.J., and Egeler, R.M. (2002). Choroid plexus
838 tumours. British journal of cancer *87*, 1086-1091.
839 Wong, C., Rougier-Chapman, E.M., Frederick, J.P., Datto, M.B., Liberati, N.T., Li, J.M., and
840 Wang, X.F. (1999). Smad3-Smad4 and AP-1 complexes synergize in transcriptional activation
841 of the c-Jun promoter by transforming growth factor beta. Mol Cell Biol *19*, 1821-1830.
842 Zawel, L., Dai, J.L., Buckhaults, P., Zhou, S., Kinzler, K.W., Vogelstein, B., and Kern, S.E. (1998).
843 Human Smad3 and Smad4 are sequence-specific transcription activators. Mol Cell *1*, 611-
844 617.
845 Zhang, J., and Li, L. (2005). BMP signaling and stem cell regulation. Developmental biology
846 *284*, 1-11.
847 Zhang, Y., Feng, X.H., and Derynck, R. (1998). Smad3 and Smad4 cooperate with c-Jun/c-Fos
848 to mediate TGF-beta-induced transcription. Nature *394*, 909-913.
849
850
851
852
853
854
855
856
857
858
859
860

861 **Figure legend**

862 *Figure 1. Prdm16 mutant ChP cells fail to exit cell cycle and are still neural progenitors*

863 (**A**) RNA *in situ* hybridization with a *Prdm16* probe, showing expression of *Prdm16* in the
864 E10.5 and E12.5 brains. The line and bracket indicate the developing ChP. (**B**) Staining of
865 PRDM16 using a PRDM16 antibody on the E13.5 control and null mutant brains. Red:
866 PRDM16; blue: the nucleus dye DAPI. White arrows indicate the ChP in the control. (**C-D**)
867 RNA in situ hybridization using a *Ttr* probe on E12.5 control and *Prdm16* null mutant brains.
868 Brain sections with tChP and hChP areas are shown separately. (**E**) Two-hour EdU labeling in
869 the E12.5 control and homozygous brains. The brain sections are co-stained with an antibody
870 against B-gal. Note: the lacZ gene trap is present in the heterozygous and homozygous mutants
871 but not in wild-type animals, and the highest expression of B-Gal is seen at the ChP indicated
872 by brackets. Red: B-Gal; blue: the nucleus dye DAPI; green: EdU. (**F**) DCX antibody staining
873 on the E12.5 control and homozygous brain slices. White arrows indicate some of the DCX
874 positive cells. Quantification of EdU+ (**E**) or DCX+ (**F**) cells is shown on the right. Biological
875 replicates: N=3. Error bars represent standard deviation (SD). Statistical significance is
876 calculated using unpaired t-test. ***, $p<0.001$.

877 *Figure 2. Prdm16 is required for BMP4-induced NSC quiescence*

878 (**A**) Illustration of the NSC culture assay. (**B**) Immunostaining of mKI67 in red and SOX2 in
879 green and EdU labeling in blue on indicated NSC genotypes and treatment. (**C**) Quantification
880 of the fraction of mKI67+ or EdU+ cells among the total cell number marked by SOX2. (**D**)
881 RT-qPCR measurement of *mKi67* RNA levels relative to 18S RNAs. Biological replicates: N=3.
882 Error bars represent standard deviation (SD). Statistical significance is calculated using
883 unpaired t-test. ***, $p<0.001$; **, p< 001; *, $p<0.05$; n.s., non-significant.

884

885 *Figure 3. PRDM16 assists genomic binding of the SMAD proteins*

886 (**A**) A Venn diagram showing the overlap of CUT&TAG peak in BMP4-treated and non-treated
887 Prdm16_E cells. **(B)** The mean coverages (normalized by library depths) centered at peak
888 summits are shown for the PRDM16 CUT&TAG signal in BMP4-treated and non-treated
889 Prdm16_E cells and Prdm16_KO mutant samples (4 replicates combined). **(C)** Heatmaps of

890 ChIP-seq coverage (normalized by library depths and input) centered at peak summits for
891 SMAD4, pSMAD1/5/8 and SMAD3 in Prdm16_E cells with or without BMP4. **(D)** Metaplots
892 of SMAD4 and pSMAD1/5/8 ChIP-seq coverage centered at SMAD or pSMAD peak summits
893 that have PRDM16 co-binding (top) and those without PRDM16 co-binding (bottom) in BMP4
894 treated *Prdm16_E* and *Prdm16_KO* cells. The average coverage is plotted in the bar plots on
895 the right. Only the peaks with PRDM16 co-binding show significant reduction in the KO cells
896 (*** P<0.001; ** P<0.01; * P<0.05; n.a. P>0.05). (**E**) The occurrence frequency of four types
897 of SMAD motifs is shown in five binned SMAD ChP-seq peaks scored from low to high. The
898 palindromic motif GTCTAGAC shows the highest occurrence frequency in peaks with
899 PRDM16 co-binding (solid red) and is the only one that has reduced occurrence frequency in
900 peaks without PRDM16 co-binding (dashed red). **(F)** A genome browser view of the *Wnt7b*
901 locus, showing PRDM16 CUT&TAG and SMAD ChIP-seq tracks. The co-bound site is
902 highlighted and shown in the enlarged view on the right. The arrows indicate ectopic SMAD
903 peaks. **(G)** ChIP-qPCR validation of SMAD4 binding to the highlighted region in *Prdm16_E*
904 and *Prdm16_KO* cells in two replicates. **(H)** A volcano plot showing differential SMAD4 ChIP-
905 seq read counts in BMP4 treated Prdm16_KO cells compared to BMP4 treated Prdm16_E cells.
906 The sites in blue are co-bound by PRDM16, while the sites in red are not bound by PRDM16
907 but within the 200kb of a PRDM16-cobound site. The average log2 fold-change is plotted on
908 the right.

909 *Figure 4. AP1 is a co-factor that associates with SMADs in the absence of Prdm16*

910 (**A-B**) *De novo* motif discovery from SMAD4 and pSMAD1/5/8 ChIP-seq peaks in *Prdm16_E*
911 cells (**A**) and *Prdm16_KO* cells (**B**). (**C**) The occurrence frequency of each indicated motif is
912 shown for SMAD4/pSMAD1/5/8 overlapped ChIP-seq peaks with or without PRDM16 co-
913 binding from BMP4 treated *Prdm16_E* cells. (**D, F**) Genome browser snapshots of the *Id3* (top)
914 and *Wnt7b* (bottom) gene loci, showing ectopic SMAD peaks in the regions, indicated by the
915 arrows. (**E, G**) ChIP-qPCR validation of increased SMAD4 and c-FOS occupancy at the
916 highlighted ectopic sites in *Prdm16_KO* mutant cells versus *Prdm16_E* cells. The locations of
917 PCR amplicons are highlighted in yellow in D and F.

918 *Figure 5. The collaborative activity of PRDM16 and SMADs represses cell proliferation genes*

919 (**A**) RT-qPCR measurement of *Wnt7b* mRNA levels in indicated genotypes and conditions from
920 three biological replicates, each with two technical replicates. Statistical significance was

921 calculated using unpaired t-test (***, p<0.001; **, p< 0.01; *, p<0.05; n.s., non-significant). (**B**)
922 Genome browser snapshots showing the H3K4me4 CUT&TAG tracks in the *Wnt7b* and
923 *Cdkn1a* loci. (**C**) A volcano plot of differential H3K4me3 read counts at TSS in Prdm16_E
924 cells with BMP4 versus those with no BMP4. Significant changes ($P < 0.01$) are colored. (**D**)
925 A volcano plot of differential H3K4me3 read counts at TSS in Prdm16_KO cells with BMP4
926 versus Prdm16_E cells with BMP4. Significant changes ($P < 0.01$) are colored. (**E**) A bubble
927 plot showing GO terms significantly enriched in SMAD-repressed genes (labelled in dark green
928 in C). **(F)** A heatmap of H3K4me3 normalized read counts at TSS of the 31 genes co-repressed
929 by PRDM16 and SMADs (overlapping genes from those in dark green in C and those in dark
930 pink in D). The genes with PRDM16 co-binding are in black text, while those without PRDM16
931 co-binding in orange. **(G)** An enhancer switch model demonstrating that SMADs change co-
932 factors and become into a transcriptional activator in the absence of PRDM16.

933 *Figure 6. PRDM16 and SMADs co-regulated genes are differentially expressed in the ChP and*
934 *neural cells*

935 (**A**) An illustration of the CH and ChP regions with opposite Wnt and BMP gradients and a
936 violin plot of scRNA-seq gene expression at E12.5 for the indicated genes in several selected
937 cell type clusters reanalyzed from (La Manno et al., 2021). Definition of the clusters is based
938 on marker gene expression from E9.5-E18.5 brain cells. These include the choroid plexus
939 clusters 1-5 (Chpl), with cluster Chpl5 identified by this study based on *Ttr* expression, Radial
940 glia clusters (RglCH 1-3, RglDF 6-10, and RglF7). CH: cortical hem; DF: dorsal forebrain; F:
941 forebrain. Per cell expression was normalized to give a log2 normalized counts. **(B)** Metaplots
942 and heatmaps of PRDM16 and IgG CUT&TAG coverage (normalized by library depths)
943 centered at peak summits from E12.5 dorsal midline tissues. **(C)** A genome browser snapshot
944 of the *Wnt7b* locus, showing PRDM16 CUT&TAG and SMADs ChIP-seq tracks.

945 *Figure 7. PRDM16 suppresses Wnt signaling and cell proliferation in the ChP epithelial cells*
946

947 (**A**) SCRINSHOT images of E11.5 wild-type and *Prdm16* mutant brains, with *BMP4*, *Ttr*,
948 *Wnt7b* and *Wnt2b* probes. Note: The red arrows indicate a strong unspecific signal in all
949 channels due to autofluorescence of blood cells. The cells selected for quantification are shown
950 together with the DAPI channel. (**B**) Enlarged views of SCRINSHOT images at the area
951 indicated in A, showing an increase of Wnt and neural gene expression levels and decrease of
952 *Ttr* and *Prdm16*. (**C**) A violin plot with the dot counts measuring expression levels of the 24

genes examined. Each gene is measured in 330 CH and 330 ChP cells from three wild-type and three Prdm16 mutant samples. (**D**) SCRINSHOT images for E12.5 wild-type and Prdm16 mutant brains, with Axin2, Ttr, Wnt 7b, Wnt2b and mKi67 probes. (**E**) Enlarged views of the areas indicated in the dash-lined rectangles in D. The ChP parts are highlighted by dashed lines. (**F**) Distribution of dot counts for indicated genes in the wild-type (*wt*) and *Prdm16* mutant (*mut*) CH and ChP areas. The X-axis shows the 110 cells in each replicate, and the Y-axis shows the mean value of the number of counts in three biological replicates. P value was calculated using area under the ROC curve in Prism Graphpad. (**G**) Multi-variant linear regression of *mKi67*, *Axin2* and *Ttr* using the dot counts for each gene in three pairs of wild-type and *Prdm16* mutant samples. All 660 cells including both CH and ChP tissues in each genotype are included. Pearson correlation and statistical difference were calculated in Prism Graphpad. (H) Illustration of the regulatory circuit, which is required for transitioning proliferative NSCs to quiescent NSCs, a prerequisite for the specification of ChP epithelial cells.

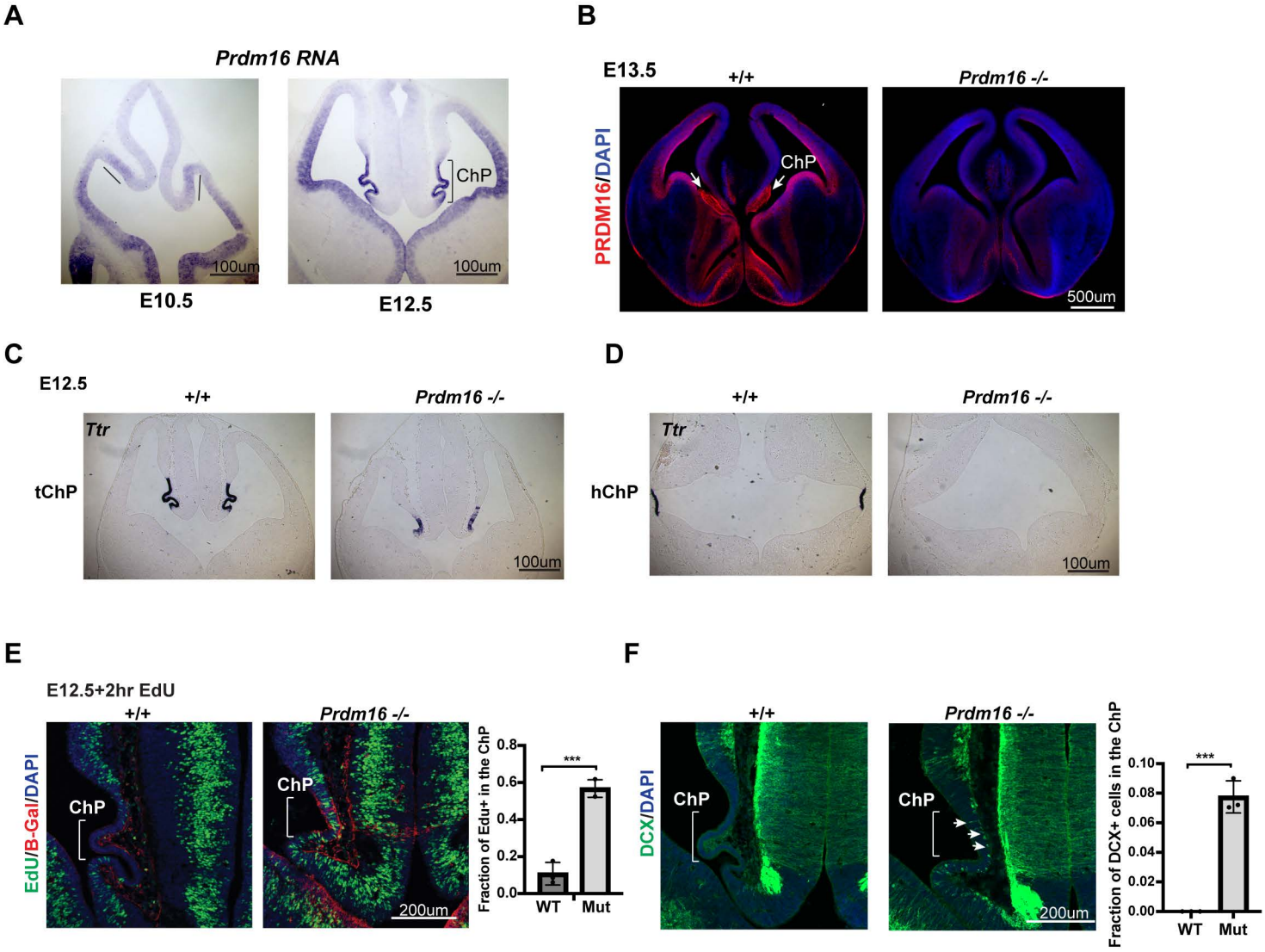
A
Prdm16 RNA
ChP
100um
100um
E10.5
E12.5
B
E13.5
+/+
Prdm16 -/-
PRDM16/DAPI
ChP
500um
C
E12.5
+/+
Prdm16 -/-
Ttr
tChP
100um
D
+/+
Prdm16 -/-
Ttr
hChP
100um
E
E12.5+2hr EdU
+/+
Prdm16 -/-
EdU/B-Gal/DAPI
ChP
ChP
200um
Fraction of Edu+ in the ChP
0.8
0.6
0.4
0.2
0.0
***
WT
Mut
F
+/+
Prdm16 -/-
DCX/DAPI
ChP
ChP
200um
Fraction of DCX+ cells in the ChP
0.10
0.08
0.06
0.04
0.02
0.00
***
WT
Mut

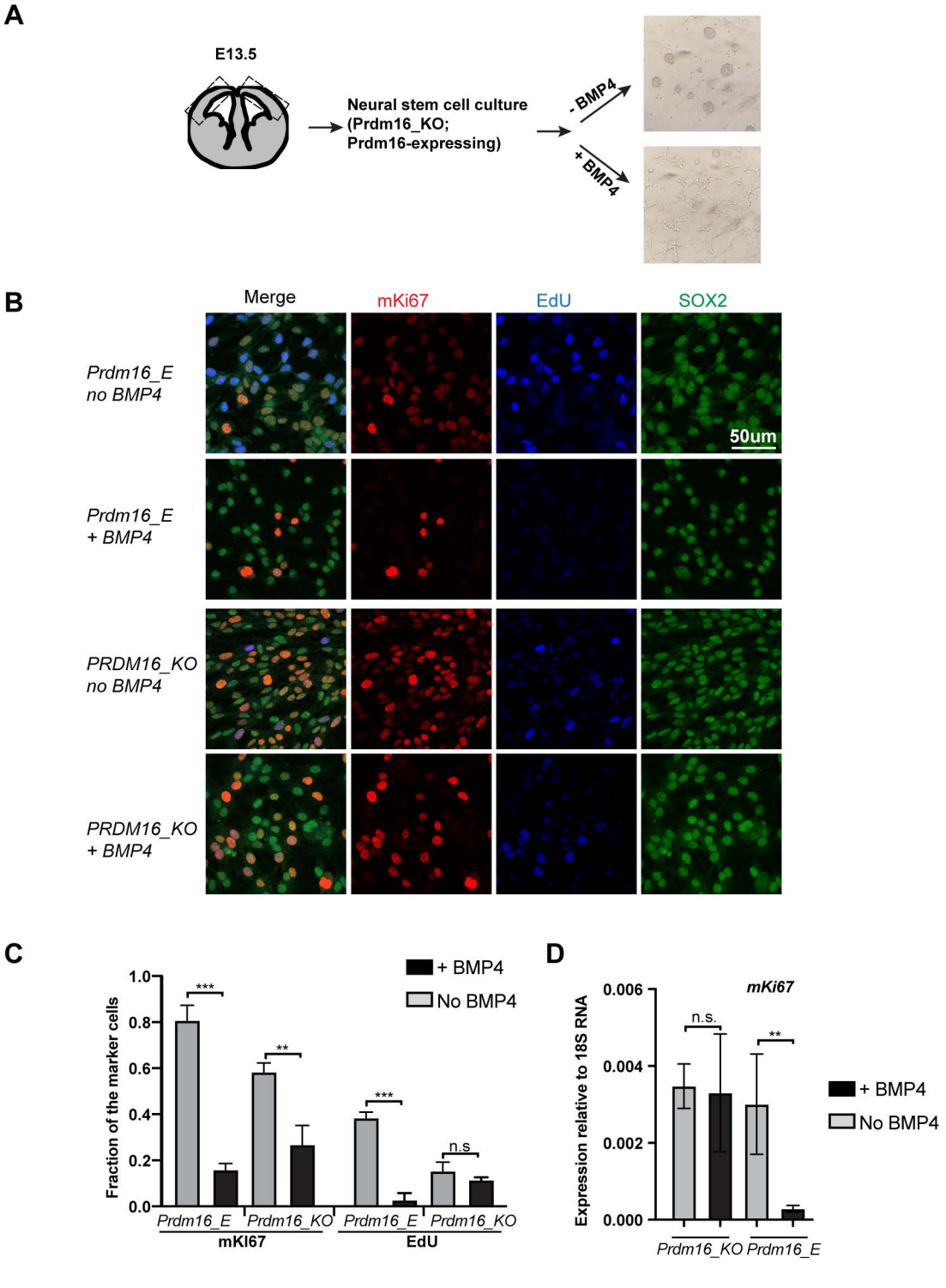
A
E13.5
Neural stem cell culture
(Prdm16_KO;
Prdm16-expressing)
- BMP4
+ BMP4
B
Merge
mKi67
EdU
SOX2
Prdm16_E
no BMP4
Prdm16_E
+ BMP4
PRDM16_KO
no BMP4
PRDM16_KO
+ BMP4
50um
C
Fraction of the marker cells
1.0
0.8
0.6
0.4
0.2
0.0
***
**
***
n.s
+ BMP4
No BMP4
Prdm16_E
Prdm16_KO
Prdm16_E
Prdm16_KO
mKI67
EdU
D
mKi67
Expression relative to 18S RNA
0.006
0.004
0.002
0.000
n.s.
**
+ BMP4
No BMP4
Prdm16_KO
Prdm16_E

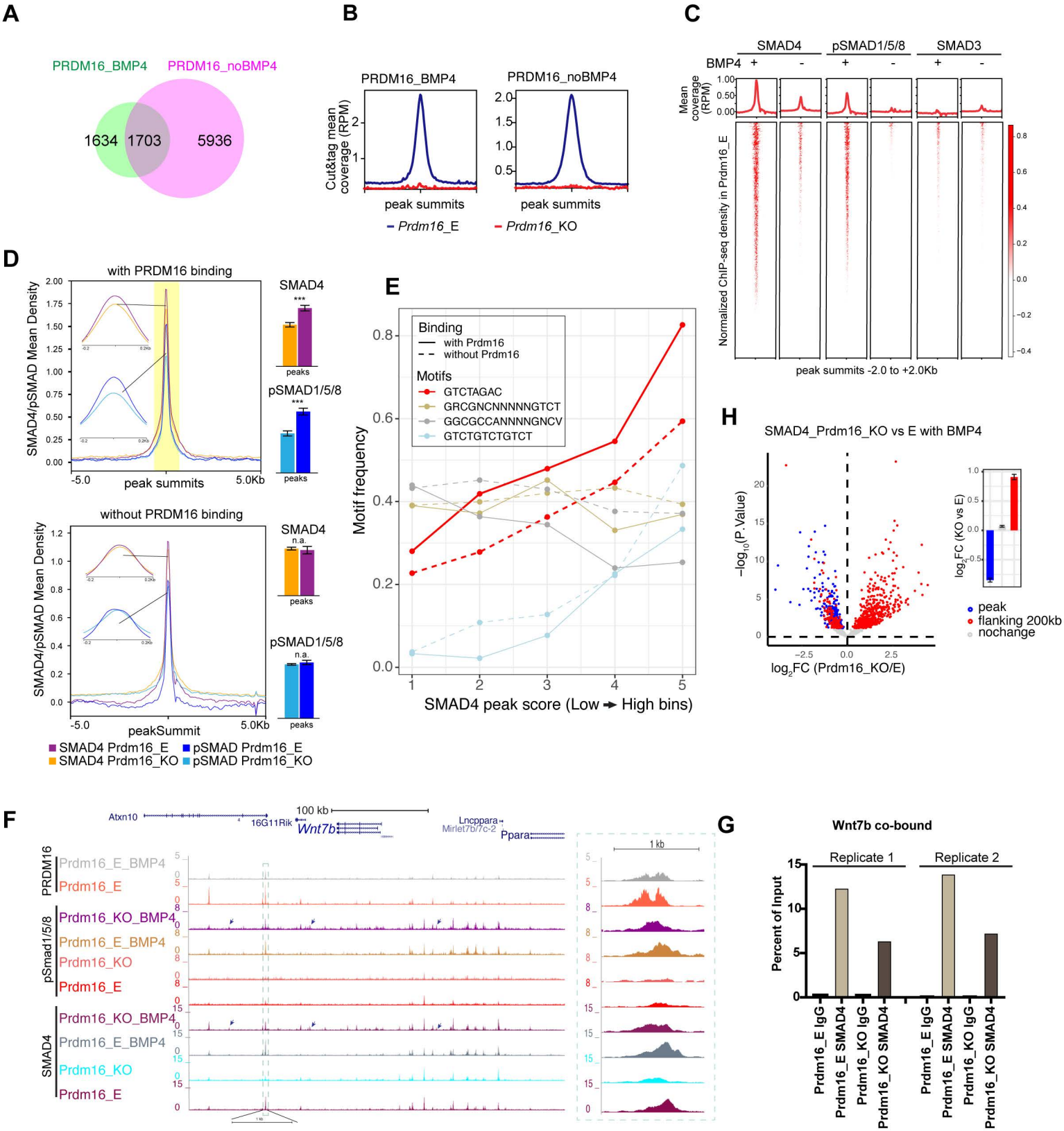
A
PRDM16_BMP4
PRDM16_noBMP4
1634
1703
5936
B
PRDM16_BMP4
PRDM16_noBMP4
Cut&tag mean coverage (RPM)
peak summits
Prdm16_E
Prdm16_KO
C
SMAD4
pSMAD1/5/8
SMAD3
BMP4
Mean coverage (RPM)
Normalized ChIP-seq density in Prdm16_E
peak summits -2.0 to +2.0Kb
D
with PRDM16 binding
SMAD4/pSMAD Mean Density
peak summits
SMAD4
pSMAD1/5/8
peaks
without PRDM16 binding
peakSummit
SMAD4 Prdm16_E
SMAD4 Prdm16_KO
pSMAD Prdm16_E
pSMAD Prdm16_KO
E
Binding
with Prdm16
without Prdm16
Motifs
GTCTAGAC
GRCGNCNNNNNGTCT
GGCGCCANNNNGNCV
GTCTGTCTGTCT
Motif frequency
SMAD4 peak score (Low → High bins)
H
SMAD4_Prdm16_KO vs E with BMP4
−log10(P.Value)
log2FC (Prdm16_KO/E)
log2FC (KO vs E)
peak
flanking 200kb
nochange
F
Atxn10
16G11Rik
Wnt7b
Lncppara
Mirlet7b/7c-2
Ppara
100 kb
1 kb
PRDM16
Prdm16_E_BMP4
Prdm16_E
pSmad1/5/8
Prdm16_KO_BMP4
Prdm16_E_BMP4
Prdm16_KO
Prdm16_E
SMAD4
Prdm16_KO_BMP4
Prdm16_E_BMP4
Prdm16_KO
Prdm16_E
G
Wnt7b co-bound
Replicate 1
Replicate 2
Percent of Input
Prdm16_E IgG
Prdm16_E SMAD4
Prdm16_KO IgG
Prdm16_KO SMAD4

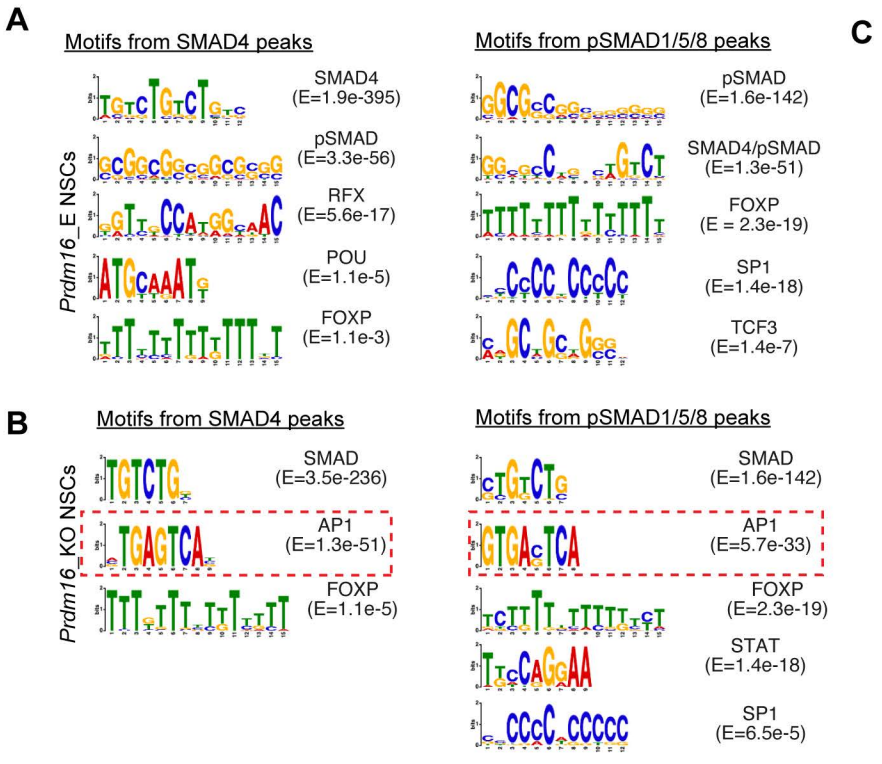
A
Motifs from SMAD4 peaks
Motifs from pSMAD1/5/8 peaks
Prdm16_E NSCs
SMAD4 (E=1.9e-395)
pSMAD (E=3.3e-56)
RFX (E=5.6e-17)
POU (E=1.1e-5)
FOXP (E=1.1e-3)
pSMAD (E=1.6e-142)
SMAD4/pSMAD (E=1.3e-51)
FOXP (E = 2.3e-19)
SP1 (E=1.4e-18)
TCF3 (E=1.4e-7)
B
Motifs from SMAD4 peaks
Motifs from pSMAD1/5/8 peaks
Prdm16_KO NSCs
SMAD (E=3.5e-236)
AP1 (E=1.3e-51)
FOXP (E=1.1e-5)
SMAD (E=1.6e-142)
AP1 (E=5.7e-33)
FOXP (E=2.3e-19)
STAT (E=1.4e-18)
SP1 (E=6.5e-5)

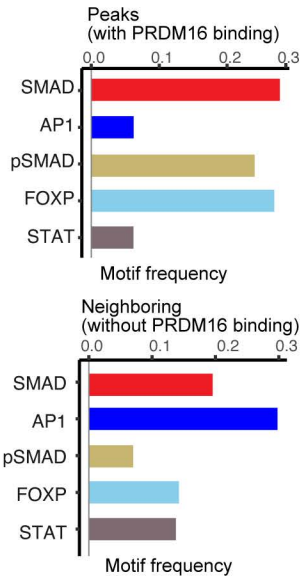
C
Peaks (with PRDM16 binding)
0.0
0.1
0.2
0.3
SMAD
AP1
pSMAD
FOXP
STAT
Motif frequency
Neighboring (without PRDM16 binding)
0.0
0.1
0.2
0.3
SMAD
AP1
pSMAD
FOXP
STAT
Motif frequency

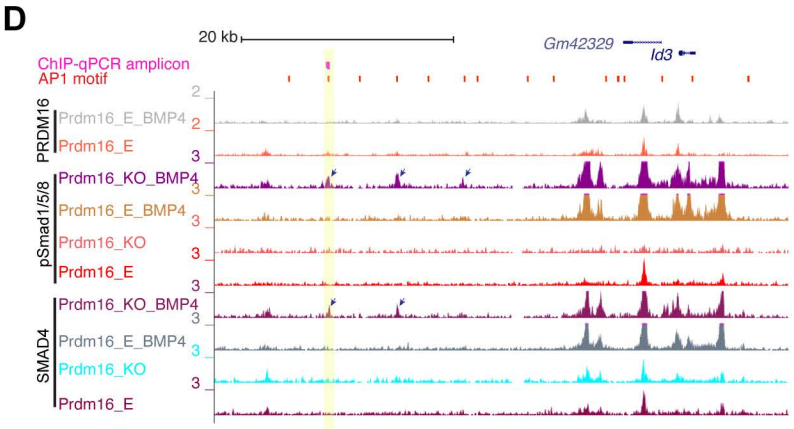
D
20 kb
Gm42329
Id3
ChIP-qPCR amplicon
AP1 motif
PRDM16
Prdm16_E_BMP4
Prdm16_E
pSmad1/5/8
Prdm16_KO_BMP4
Prdm16_E_BMP4
Prdm16_KO
Prdm16_E
SMAD4
Prdm16_KO_BMP4
Prdm16_E_BMP4
Prdm16_KO
Prdm16_E

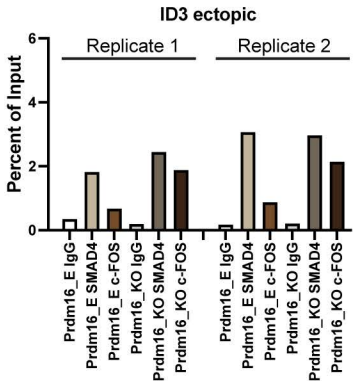
E
ID3 ectopic
Replicate 1
Replicate 2
Percent of Input
0
2
4
6
Prdm16_E IgG
Prdm16_E SMAD4
Prdm16_E c-FOS
Prdm16_KO IgG
Prdm16_KO SMAD4
Prdm16_KO c-FOS
Prdm16_E IgG
Prdm16_E SMAD4
Prdm16_E c-FOS
Prdm16_KO IgG
Prdm16_KO SMAD4
Prdm16_KO c-FOS

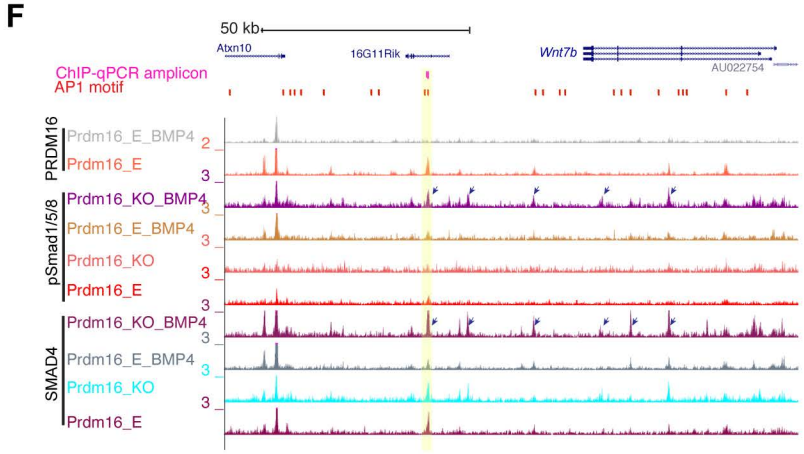
F
50 kb
Atxn10
16G11Rik
Wnt7b
AU022754
ChIP-qPCR amplicon
AP1 motif
PRDM16
Prdm16_E_BMP4
Prdm16_E
pSmad1/5/8
Prdm16_KO_BMP4
Prdm16_E_BMP4
Prdm16_KO
Prdm16_E
SMAD4
Prdm16_KO_BMP4
Prdm16_E_BMP4
Prdm16_KO
Prdm16_E

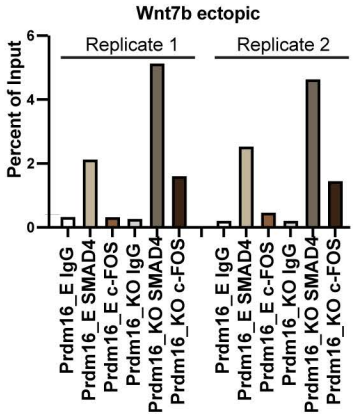
G
Wnt7b ectopic
Replicate 1
Replicate 2
Percent of Input
0
2
4
6
Prdm16_E IgG
Prdm16_E SMAD4
Prdm16_E c-FOS
Prdm16_KO IgG
Prdm16_KO SMAD4
Prdm16_KO c-FOS
Prdm16_E IgG
Prdm16_E SMAD4
Prdm16_E c-FOS
Prdm16_KO IgG
Prdm16_KO SMAD4
Prdm16_KO c-FOS

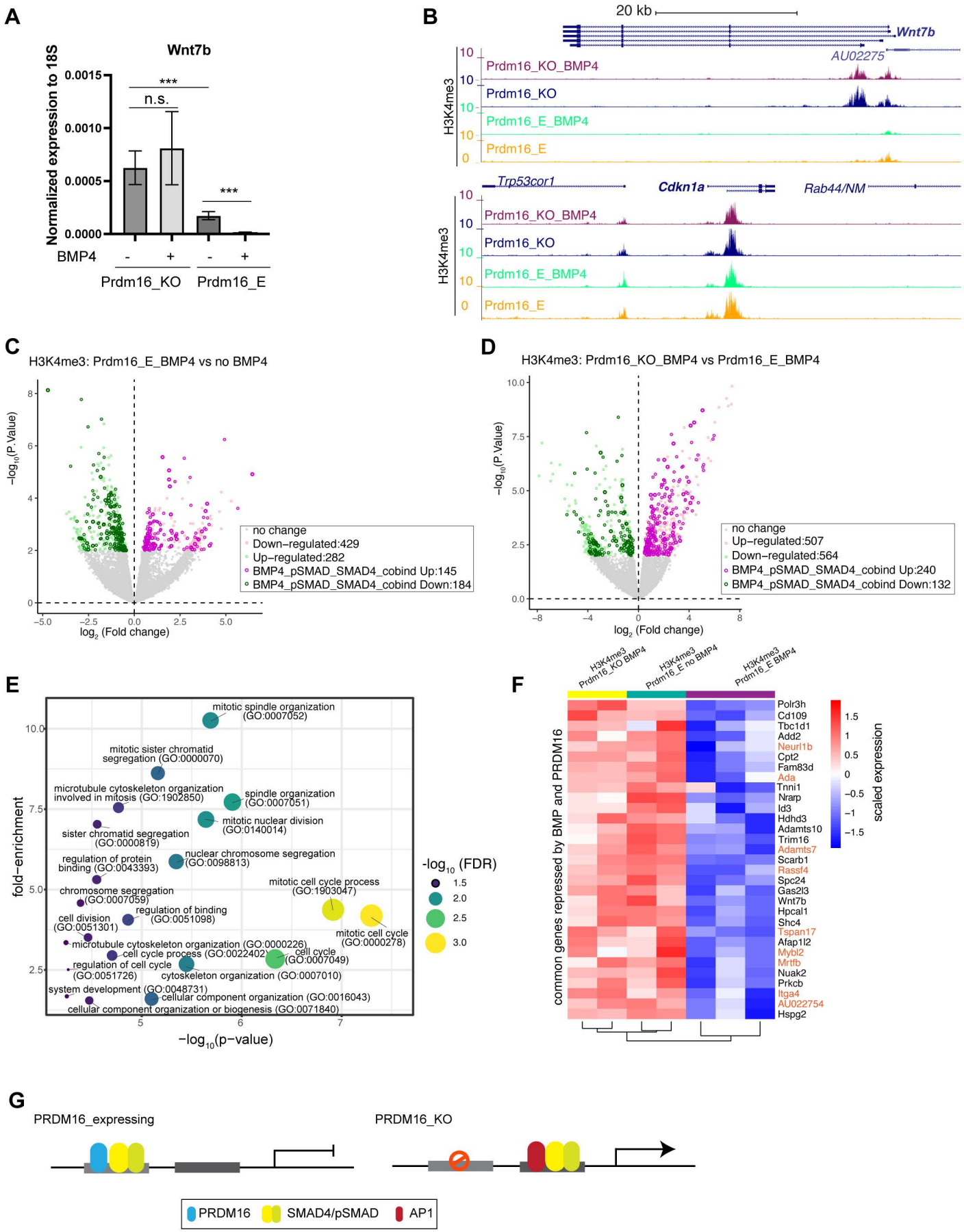
A
Wnt7b
Normalized expression to 18S
0.0015
0.0010
0.0005
0.0000
***
n.s.
***
BMP4
-
+
-
+
Prdm16_KO
Prdm16_E
B
20 kb
Wnt7b
AU02275
H3K4me3
Prdm16_KO_BMP4
Prdm16_KO
Prdm16_E_BMP4
Prdm16_E
Trp53cor1
Cdkn1a
Rab44/NM
C
H3K4me3: Prdm16_E_BMP4 vs no BMP4
−log10(P.Value)
log2 (Fold change)
no change
Down−regulated:429
Up−regulated:282
BMP4_pSMAD_SMAD4_cobind Up:145
BMP4_pSMAD_SMAD4_cobind Down:184
D
H3K4me3: Prdm16_KO_BMP4 vs Prdm16_E_BMP4
−log10(P.Value)
log2 (Fold change)
no change
Up−regulated:507
Down−regulated:564
BMP4_pSMAD_SMAD4_cobind Up:240
BMP4_pSMAD_SMAD4_cobind Down:132
E
mitotic spindle organization (GO:0007052)
mitotic sister chromatid segregation (GO:0000070)
microtubule cytoskeleton organization involved in mitosis (GO:1902850)
spindle organization (GO:0007051)
mitotic nuclear division (GO:0140014)
sister chromatid segregation (GO:0000819)
regulation of protein binding (GO:0043393)
nuclear chromosome segregation (GO:0098813)
mitotic cell cycle process (GO:1903047)
chromosome segregation (GO:0007059)
regulation of binding (GO:0051098)
cell division (GO:0051301)
mitotic cell cycle (GO:0000278)
microtubule cytoskeleton organization (GO:0000226)
cell cycle process (GO:0022402)
cell cycle (GO:0007049)
regulation of cell cycle (GO:0051726)
cytoskeleton organization (GO:0007010)
system development (GO:0048731)
cellular component organization (GO:0016043)
cellular component organization or biogenesis (GO:0071840)
fold−enrichment
−log10(p−value)
-log10 (FDR)
1.5
2.0
2.5
3.0
F
H3K4me3 Prdm16_KO BMP4
H3K4me3 Prdm16_E no BMP4
H3K4me3 Prdm16_E BMP4
common genes repressed by BMP and PRDM16
Polr3h
Cd109
Tbc1d1
Add2
Neurl1b
Cpt2
Fam83d
Ada
Tnni1
Nrarp
Id3
Hdhd3
Adamts10
Trim16
Adamts7
Scarb1
Rassf4
Spc24
Gas2l3
Wnt7b
Hpcal1
Shc4
Tspan17
Afap1l2
Mybl2
Mrtfb
Nuak2
Prkcb
Itga4
AU022754
Hspg2
scaled expression
G
PRDM16_expressing
PRDM16_KO
PRDM16
SMAD4/pSMAD
AP1

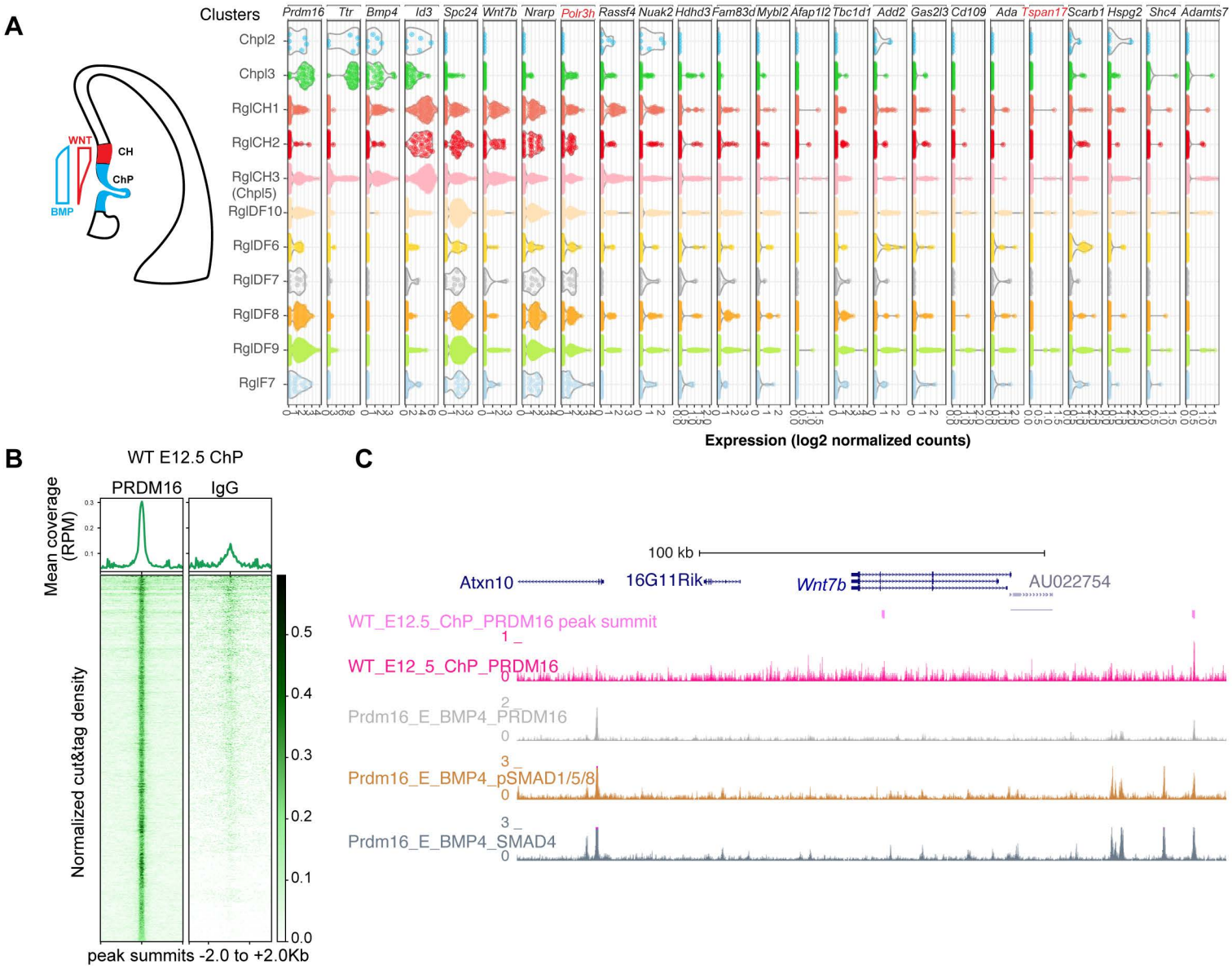
A
Clusters
Prdm16
Ttr
Bmp4
Id3
Spc24
Wnt7b
Nrarp
Polr3h
Rassf4
Nuak2
Hdhd3
Fam83d
Mybl2
Afap1l2
Tbc1d1
Add2
Gas2l3
Cd109
Ada
Tspan17
Scarb1
Hspg2
Shc4
Adamts7
Chpl2
Chpl3
RglCH1
RglCH2
RglCH3
(Chpl5)
RglDF10
RglDF6
RglDF7
RglDF8
RglDF9
RglF7
WNT
CH
ChP
BMP
Expression (log2 normalized counts)
B
WT E12.5 ChP
PRDM16
IgG
Mean coverage
(RPM)
Normalized cut&tag density
peak summits -2.0 to +2.0Kb
C
100 kb
Atxn10
16G11Rik
Wnt7b
AU022754
WT_E12.5_ChP_PRDM16 peak summit
WT_E12_5_ChP_PRDM16
Prdm16_E_BMP4_PRDM16
Prdm16_E_BMP4_pSMAD1/5/8
Prdm16_E_BMP4_SMAD4

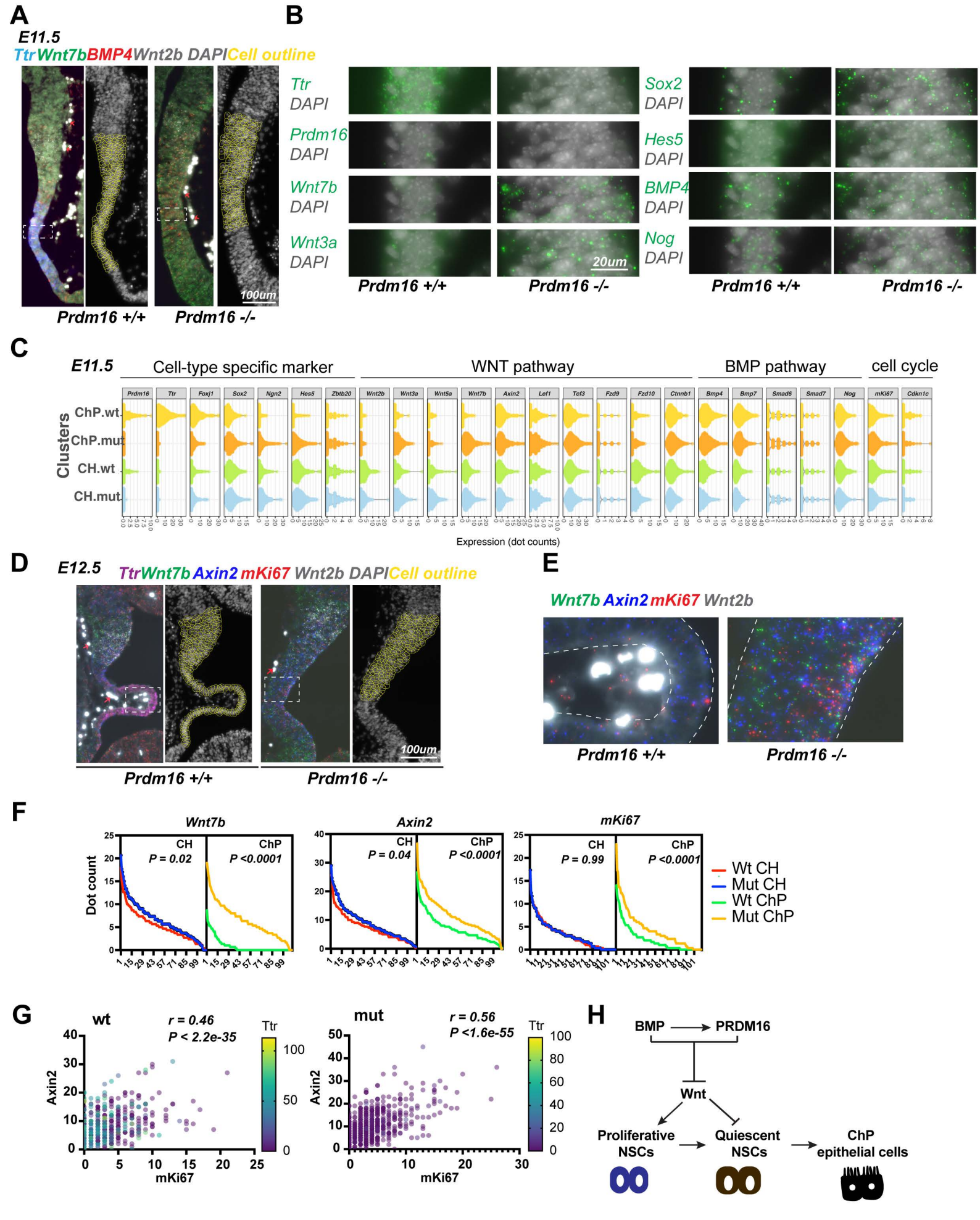
A
E11.5
Ttr Wnt7b BMP4 Wnt2b DAPI Cell outline
100um
Prdm16 +/+
Prdm16 -/-
B
Ttr DAPI
Prdm16 DAPI
Wnt7b DAPI
Wnt3a DAPI
Sox2 DAPI
Hes5 DAPI
BMP4 DAPI
Nog DAPI
20um
Prdm16 +/+
Prdm16 -/-
Prdm16 +/+
Prdm16 -/-
C
E11.5
Cell-type specific marker
WNT pathway
BMP pathway
cell cycle
Prdm16 Ttr Foxj1 Sox2 Ngn2 Hes5 Zbtb20 Wnt2b Wnt3a Wnt5a Wnt7b Axin2 Lef1 Tcf3 Fzd9 Fzd10 Ctnnb1 Bmp4 Bmp7 Smad6 Smad7 Nog mKi67 Cdkn1c
Clusters
ChP.wt
ChP.mut
CH.wt
CH.mut
Expression (dot counts)
D
E12.5
Ttr Wnt7b Axin2 mKi67 Wnt2b DAPI Cell outline
100um
Prdm16 +/+
Prdm16 -/-
E
Wnt7b Axin2 mKi67 Wnt2b
Prdm16 +/+
Prdm16 -/-
F
Wnt7b
Axin2
mKi67
Dot count
CH
P = 0.02
ChP
P <0.0001
CH
P = 0.04
ChP
P <0.0001
CH
P = 0.99
ChP
P <0.0001
Wt CH
Mut CH
Wt ChP
Mut ChP
G
wt
r = 0.46
P < 2.2e-35
Ttr
Axin2
mKi67
mut
r = 0.56
P <1.6e-55
Ttr
Axin2
mKi67
H
BMP
PRDM16
Wnt
Proliferative NSCs
Quiescent NSCs
ChP epithelial cells